MNRAS **000**, 000–000 (2018) Preprint 2 August 2018 Compiled using MNRAS LATEX style file v3.0

The GALAH survey and *Gaia* DR2: forced oscillation and phase mixing in the local stellar disc

Joss Bland-Hawthorn[1,2,3]★, Sanjib Sharma[1,2], Thor Tepper-Garcia[1], James Binney[4], Ken C. Freeman[5], Michael R. Hayden[1,2], Geraint F. Lewis[1], Janez Kos[1], Gayandhi M. De Silva[1,6], Martin Asplund[2,5], Sven Buder[7,8], Ly Duong[5], Jane Lin[5], Karin Lind[9], Sarah L. Martell[10], Melissa K. Ness[11,12], Katharine J. Schlesinger[5], Jeffrey D. Simpson[6], Daniel B. Zucker[6], Tomaž Zwitter[13], and the GALAH team
(Affiliations listed after the references)

2 August 2018

ABSTRACT

Spectacular evidence of a coherent pattern in phase space has emerged in the local stellar disc from an analysis of 6 million stars in the ESA *Gaia* Data Release 2 (*Gaia* DR2). This remarkable astrometric mission is complemented by the ongoing GALAH survey of the Milky Way that exploits the HERMES high-resolution ($\mathcal{R} \approx 28,000$), multi-object spectrograph at the Anglo-Australian Telescope. In its latest release, GALAH DR2 provides accurate radial velocities ($\sigma_{rv} \approx 0.1 - 0.2$ km s^{-1}) and stellar abundances (for up to 23 elements) for 342,682 stars, all of which overlap with the *Gaia* catalogue. If (V_R, V_ϕ, V_z) are the components of velocity in Galactic cylindrical coordinates (R, ϕ, z), the phase-wrapping signature is seen most clearly in the vertical phase plane (z, V_z) when averaging over V_ϕ for all *Gaia* stars in the local volume element as a function of the phase space coordinates, i.e. $\langle V_\phi(z, V_z)\rangle$. A weaker spiral phase is also seen in the $\langle V_R(z, V_z)\rangle$ plane superimposed on a quadrupole pattern due to the tilt of the local velocity ellipsoid. The one-arm ($m = 1$) spiral trajectory in phase space (which we abbreviate to 'spiral phase') is recovered by the GALAH (and LAMOST) survey in both the thin disc and thick disc population defined in the [Fe/H] vs. [α/Fe] plane. The stellar abundances moving out from the centre of the 3D spiral phase reflect the vertical and radial metallicity gradients. We conduct simulations of the Milky Way being hit by the Sgr dwarf using a range of impactor masses ($1 - 10 \times 10^{10}$ M$_\odot$), all of which lose mass and cross the disc multiple times. In regions where the disc-crossing timescale (τ_C) is comparable to the disc's vertical period ($\tau_C \sim 2\pi/\omega_z$), Sgr drives a forced oscillation in the disc population resulting in 'bending waves' across the disc. This produces a rotating spiral pattern in the (z, V_z) plane seen in both V_R and V_ϕ that does not wind up on large scales. At smaller radii and close to the disc plane for which $\tau_C \ll 2\pi/\omega_z$, phase-wrapping and mixing does occur. The amplitude and contrast of the phase pattern observed today is consistent with an impactor mass of at least 3×10^{10} M$_\odot$ at transit stripped down from 5×10^{10} M$_\odot$when it crossed the virial radius. Each successive disc transit washes out the spiral phase signal but it reforms in about 100 – 150 Myr before the next crossing. Since the last crossing occurred about 400 Myr ago, the spiral phase cannot be older than about 250 – 300 Myr.

Key words: Surveys – the Galaxy – stars: abundances – stars: dynamics – stars: kinematics

]

1 INTRODUCTION

The ESA *Gaia* astrometric mission (Perryman et al. 2001; Prusti et al. 2016) has been eagerly anticipated for many years by the stellar and Galactic communities and the early results have not disappointed (DR2: Brown et al. 2018). Wide-field stellar surveys across the Galaxy are fundamental to astrophysics because there are important measurements that can only be made in the near-field.

★ Contact e-mail: jbh@physics.usyd.edu.au

The remarkable precision of measured stellar parameters by *Gaia* after only two years of observations has triggered a flurry of new discoveries and new fields of study (e.g. Antoja et al. 2018; Eyer et al. 2018; Marchetti et al. 2018; Koppelman et al. 2018; Malhan et al. 2018). Complementary stellar surveys (RAVE, APOGEE, LAMOST, Gaia-ESO, K2) are now able to exploit the overlap of targets with *Gaia* DR2 – this is the golden age of Galactic archaeology (Freeman & Bland-Hawthorn 2002).

Our focus here is on the synergy between *Gaia* and the Galactic Archaeology with HERMES (GALAH)[1] survey based at the Anglo-Australian Telescope (AAT) in Australia. This survey brings a unique perspective to Galactic archaeology by measuring accurate radial velocities and up to 30 elemental abundances (more for the brightest stars) for about a million stars (De Silva et al. 2015; Martell et al. 2017). The HERMES instrument was designed and optimised for the GALAH survey specifically for the pursuit of Galactic archaeology (Freeman & Bland-Hawthorn 2008; Barden et al. 2010). The GALAH selection criteria were designed to be as simple as possible to avoid problems that adversely affect earlier surveys (Sharma et al. 2011). The primary selection is based on a magnitude range of $12 < V < 14$ and a cut in Galactic latitude, $|b| > 10$ deg. Thus GALAH probes mainly the thin and thick discs of the Galaxy. The impact of *Gaia* was a key consideration from the outset, particularly with regard to choosing a bright limiting magnitude to ensure good distances for all stars.

The second GALAH data release (GALAH DR2) features stellar parameters, radial velocities and up to 23 elemental abundances for 342,682 stars (Buder et al. 2018). All of these stars have complementary data from the *Gaia* DR2 data archive. GALAH's high-quality radial velocities, with mean errors of $0.1-0.2$ km s^{-1} (Zwitter et al. 2018), are much better than the *Gaia* radial velocities, but comparable to or better than typical transverse velocities derived from the proper motions (Brown et al. 2018). The GALAH-*Gaia* synergy[2] is particularly strong for local dwarfs which dominate the survey within about 1 kpc. We exploit this advantage in the present study.

Our work is inspired by the remarkable discovery of a 6D phase-space signal in the local stellar disc by the *Gaia* team (Antoja et al. 2018). It has long been recognized that a confined group of stars in moving in phase space constitutes an incompressible flow governed by the Boltzmann equation that becomes more distorted (wrapped) as it evolves (Lynden-Bell 1967). The fine-grained density is preserved but the coarse-grained density evolves towards an equilibrium state. In a volume element defined by $(\Delta R, \Delta\phi, \Delta z) = (\pm 0.1, \pm 0.1, \pm 1)$ kpc^3 centred on the Sun, Antoja et al. (2018) detect a coherent spiral pattern in the local 6D phase space. This phenomenon occurs in a system which is attempting to relax from a mildly disturbed state to a stationary configuration.

After Antoja et al. (2018), we adopt velocity components (V_R, V_ϕ, V_z) in Galactic cylindrical coordinates (R, ϕ, z). The spiral phase is particularly prominent in a plane defined by $\langle V_\phi(z, V_z)\rangle$ where $\langle V_\phi\rangle$ is an average value of V_ϕ for all stars in the volume element at a given location in (z, V_z). The *Gaia* team also presented the mapping $\langle V_R(z, V_z)\rangle$ but the full import of this result appears to have gone unnoticed, as we discuss. What is immediately apparent are the special conditions required for the unanticipated spiral phase to be evident. The one-arm spiral phase undergoes at least three wraps ($\gtrsim 6\pi$) in the (z, V_z) plane indicating a time-dependent or a time-variable response within the local disk. At one or more times in the past, some stars were forced into a narrow phase interval along their orbits. The spiral phase population must be compressed enough in phase space so as not to smear out the signature.

The disc's response to a quasi-impulsive transiting, massive object is a natural mechanism to induce incomplete phase mixing in the local stellar population. Antoja et al. (2018) considered the impact of the Sgr dwarf and inferred timescales for the event based on the tangent points of the phase-wrapped signal. Other temporal phenomena are possible. For example, Sgr may have triggered a starburst in the solar neighbourhood; since most star clusters disrupt within 100 Myr, these populations defined initially by a compact cloud in phase space are then free to oscillate in the disc potential (Candlish et al. 2014). Alternatively, disc bending modes or corrugations can be excited by halo substructure (e.g. Chequers et al. 2018) or the close passage of a perturber like Sgr (Gómez et al. 2015). Resonant high latitude, stellar populations can build up during the disc's growth (e.g. levitating orbits, Sridhar & Touma 1996), or transient behaviour associated with accretion (Sellwood & Carlberg 1984; Bland-Hawthorn & Sharma 2016), the bar, the spiral arms or the outer warp (Hunter & Toomre 1969; Masset & Tagger 1997a,b; Sellwood & Carlberg 2014). Some of these mechanisms are ruled out because they possess a symmetry — $(z, V_z) = (-z, V_z)$, or $(z, V_z) = (-z, -V_z)$, etc. — that is not observed, as we discuss.

In order to arrive at a deeper understanding of the new phase space signal, we extend the analysis of the spiral phase over larger volumes, using more precise radial velocities, and stellar abundance parameters for the first time provided by the GALAH survey. We look at stars that are common to both *Gaia* DR2 and GALAH DR2. In Section 2, we form the union of the GALAH and *Gaia* surveys, and make further selections and improvements. In Section 3, a new analysis of the spiral phase is given first for the *Gaia* data and then supplemented by the GALAH and LAMOST data. For all surveys, the signature is remarkably clear. In Section 4, we discuss the GALAH data and the spiral phase in terms of inferred actions for the first time. In Section 5, we present a short discussion of the velocity ellipsoid evident in the GALAH and *Gaia* data. In Section 6, some dynamical implications are considered prior to a search, in Section 7, for the spiral phase signal in our new simulations of Sgr impacting the Galactic disc. Section 8 gives an overview of the new work and provides some pointers to future work.

2 GALAH OBSERVATIONS AND GAIA OVERLAP

2.1 Reference frame

Our adopted conventions are righthanded systems for the heliocentric and Galactocentric reference frames. The Solar motion $\mathbf{v}_{\rm LSR}$ is the peculiar motion defined with respect to the Local Standard of Rest (LSR). The circular motion of the LSR (Θ_0) is defined in the Galactic plane along a circular orbit centred on Sgr A* that passes through the Sun's position today. For a system tied to the Sun, where the $\mathbf{i}$ unit vector points towards the Galactic Centre, $\mathbf{j}$ in the direction of rotation, and $\mathbf{k}$ is towards the North Galactic Pole (NGP), $\mathbf{v}_{\rm LSR} = U_\odot\mathbf{i} + V_\odot\mathbf{j} + W_\odot\mathbf{k}$. For a location defined by $\mathbf{r} = x\mathbf{i} + y\mathbf{j} + z\mathbf{k}$, we place Sgr A* at $(x, y, z) = (R_\odot, 0, -z_\odot)$ kpc where $R_\odot = 8.2 \pm 0.1$ kpc and $z_\odot = 25$ pc (Bland-Hawthorn & Gerhard 2016) consistent with the new ESO Gravity measurement (Gravity Collaboration et al. 2018).

[1] https://galah-survey.org/

[2] The power of this synergy is demonstrated by (Kos et al. 2018) who reveal that four well known NGC "open clusters" first identified in 1888 are projections and not physical systems. This required the velocity vector of each star to be measured to better than 0.5 km s^{-1}.

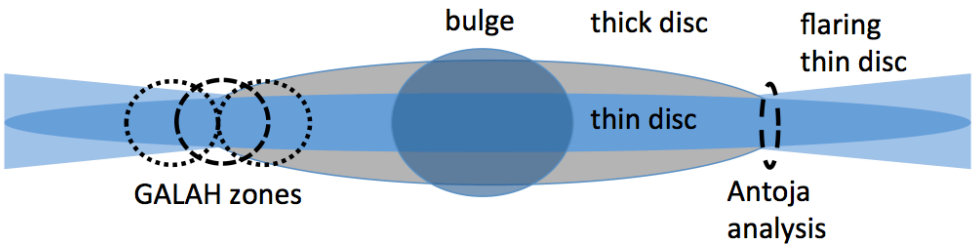

Figure 1. Schematic diagram of the modern interpretation of the thick disc based on the APOGEE survey (Hayden et al. 2015). The thick disc has a shorter scalelength than the thin disc and terminates near the Solar Circle. Here, the thin disc takes over and begins to flare at larger radius. The thin vertical ellipse shows the extent of the Antoja et al. (2018) *Gaia* analysis; the large dashed and dotted circles show the domain of our analysis. Both studies were performed in the solar neighbourhood. The transition from thick disc to flaring thin disc is exaggerated for illustration. The stellar metallicity declines with both R and z increasing everywhere across the Galaxy.

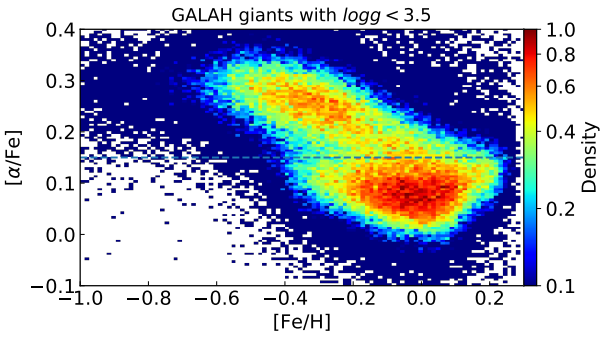

Figure 2. Distribution of giants in the [Fe/H] vs. [α/Fe] plane using data from GALAH survey. Giants were selected with $\log g < 3.5$. A clear separation of the high and low [α/Fe] populations is visible. The boundary line distinguishing the high and low [α/Fe] populations is shown (cf. Adibekyan et al. 2012).

As seen from the NGP looking towards the disc, we define Galactocentric cylindrical coordinates centred at Sgr A* using (R, ϕ, z). Here ϕ is measured in the clockwise direction with the Sun at $\phi_\odot = 180°$ to ensure the Sun's motion has positive V_ϕ (Antoja et al. 2018). R is measured outwards such that V_R is positive in the same sense; z increases in the direction of the NGP and V_z is positive in the same sense. To convert velocities from the heliocentric to the Galactocentric frame, we adopt the angular velocity of the Sun $\Omega_\odot$ $(= (\Theta_0 + V_\odot)/R_\odot)$ with respect to the Galactic Centre as 30.24 km s^{-1} kpc^{-1} using the reflex (proper) motion of Sgr A* (Reid & Brunthaler 2004), the Sun's peculiar motion as $V_\odot = 10.0$ km s^{-1} such that $v_\odot = 238$ km s^{-1} (Bland-Hawthorn & Gerhard 2016). We ignore any further correction to $\mathbf{v}_{\rm LSR}$ for streaming motions with respect to the LSR (e.g. Sharma et al. 2014; Gravity Collaboration et al. 2018).

2.2 *Gaia* overlap

Antoja et al. (2018) focussed their *Gaia* DR2 study on stars that are close to the Sun in the plane of the Galaxy, confining their sample to $|R - R_\odot| \leqslant 0.1$ kpc and $|\phi - \phi_\odot| \leqslant 7.5°$. To revisit the spiral phase in more detail, we expand the volume by an order of magnitude to $|R - R_\odot| \leqslant 1.0$ kpc and $|\phi - \phi_\odot| \leqslant 15°$. This aids comparison with a higher number of GALAH stars. After Antoja et al. (2018), we provide an additional cut on parallax ϖ to ensure good distances, i.e. $\sigma_\varpi/\varpi < 0.2$, which is sufficient for the scope of our analysis. The domain of both studies is shown in Figure 1.

2.3 GALAH observations

The GALAH survey exploits the High Efficiency and Resolution Multi-Element Spectrograph (HERMES) at the Anglo-Australian Telescope (Sheinis et al. 2015). This unique instrument employs the Two Degree Field (2dF) fibre positioner at the f/3.3 Prime Focus to provide multi-object ($n \approx 400$), high-resolution ($\mathcal{R} \approx 28,000$) spectra of many stars in a single shot. HERMES is a fibre-fed, multi-channel spectrograph optimised to carry out Galactic archaeology from a 4m-class telescope (De Silva et al. 2015). HERMES has four optical spectrographs covering 471–490 nm, 564–587 nm, 647–673 nm and 758–788 nm for determining elemental abundances for up to 30 elements per star (up to 45 elements for the brightest stars).

Here we use the internal data release of 505571 stars provided to the GALAH team which includes GALAH DR2 (Buder et al. 2018) augmented with HERMES data from parallel observations of open clusters, K2 (Wittenmyer et al. 2018) and TESS fields (Sharma et al. 2018). These new observations, which provide improved calibrations of stellar masses and gravities, were reduced with the same pipeline used in DR2 (Kos et al. 2017). The additional numbers of stars are 2498, 97133 and 42764 respectively. From this sample, we select stars with the GAIA DR2 relative parallax uncertainty of less than 20% and radial distance $|R - R_\odot| \leqslant 1.0$ and $|\phi - \phi_\odot| \leqslant 15°$. This resulted in a sample of 192972 stars.

We separate the stars into different metallicity bins defined by [Fe/H] and [α/Fe]. In the first analysis, we examine the spiral phase in terms of metal rich and metal poor populations using only [Fe/H]. In the second analysis, we use the simplest possible separation in ([Fe/H], [α/Fe]) as indicated in Fig. 2, consistent with the break and distinct kinematic properties observed in Büdenbender et al. (2015, Fig. 3). This is a simpler definition than the stepped function used by Adibekyan et al. (2012) but the results are basically the same for either choice of thin-thick disc separation. Our simple cut does a good job of separating the two sequences as confirmed by the kinematic properties. In order to aid a meaningful comparison, the maps that follow in Section 2 are constructed using comparable numbers of stars, as indicated in the separate panels. This was done by randomly subsampling the population of stars for each case.

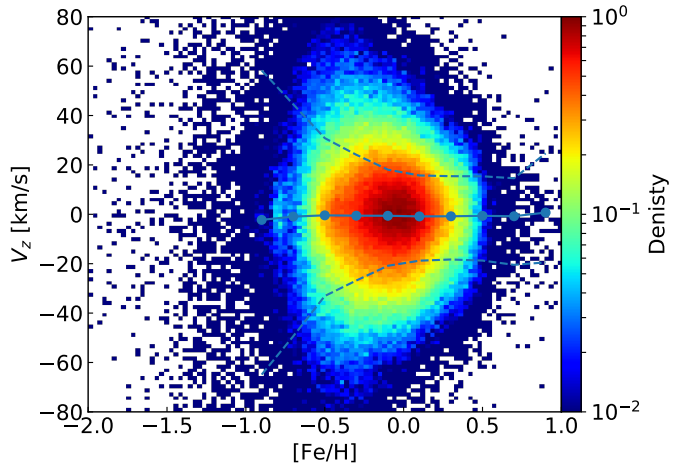

Figure 3. The trend in [Fe/H] vs. V_z colour coded in terms of relative density per pixel. [Fe/H] is taken from the GALAH survey; V_z is determined from *Gaia* proper motions and GALAH radial velocities. The mean trend is indicated; the 1σ error tracks show the progression from the thin disc to the thick disc and halo as [Fe/H] declines. This is important for understanding the visibility of the spiral phase appears in different metallicity bins.

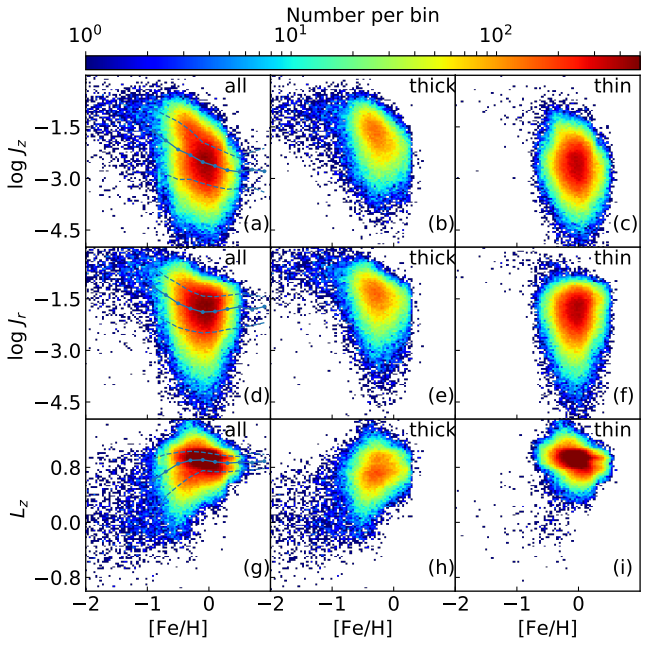

Figure 4. Stellar metallicity vs. actions for overlapping stars between GALAH and *Gaia* DR2 in the 2-kpc diameter volume (Figure 1); the normalised stellar densities are shown in colour. All actions are normalised by the factor $R_\odot v_\odot$. The left column is for all stars, the middle column for the thick disc, and the right column for the thin disc. (a-c) [Fe/H] vs. $J \log J_z$, (d-f) [Fe/H] vs. $\log J_R$, (g-i) [Fe/H] vs. $J_\phi \equiv L_z$. The mean trend and 1σ dispersion tracks are also shown in the first column. Note the trend from the cold, rotating thin disc in (i) at high [Fe/H] to the slower thick disc in (h) and, below [Fe/H]=-0.6, the metal-poor halo supported by pressure (high J_z, J_R in (b), (e)). The L_z split visible in (g) and (i) reflects kinematic substructure within the data.

3 SPIRAL PHASE SIGNATURE

3.1 *Gaia* analysis

3.1.1 Spiral implications

Antoja et al. (2018) were the first to reveal the spiral pattern in the vertical phase plane (z, V_z). The phase-wrapped signature is seen most clearly when averaging over V_ϕ for all *Gaia* stars in the local volume element as a function of the phase space coordinates, i.e. $\langle V_\phi(z, V_z)\rangle$. To aid the discussion, we adopt action-angle variables where the actions are given by $\mathbf{J}(J_R, J_\phi{=}L_z, J_z)$, for which L_z is the angular momentum about the z axis, and the angles are given by $\Theta(\theta_R, \theta_\phi, \theta_z)$. For a system in quasi-equilibrium, actions are integrals of motion (adiabatic invariants) along the orbit. Sanders (2012) gives explicit formulae for the separable Stäckel potential but they can be numerically computed for any potential. The actions measure the extent of the oscillation in the respective variable (Section 4). In Figure 4, this is beautifully illustrated when we combine the GALAH metallicities and *Gaia* DR2 actions (see section 4 for further details). Above solar [Fe/H], the stars have L_z near unity (circular rotation) with characteristically lower values of J_R and J_z. Below about [Fe/H] ≈ -0.6, the metal-poor stellar halo picks up. Here the radial and vertical actions reach their peak in support of the halo's dynamical pressure (cf. Figure 3).

In Figure 5a, we recover Antoja's original $\langle V_\phi\rangle$ signature in the vertical phase plane. A weaker spiral phase is also seen in the $\langle V_R(z, V_z)\rangle$ plane, discussed in detail in a later section. The spiral pattern is barely visible in projected stellar density $\mu_\star(z, V_z)$ over the same volume. The key point is that there is a manifest correlation between the in-plane and vertical motions which is telling us something important about galaxy dynamics. The similar patterns observed between $\langle V_R\rangle$ and $\langle V_\phi\rangle$ are presumably a consequence of the strong in-plane epicyclic motion (e.g. Equation 3.102; Binney & Tremaine 2008); see also (Binney & Schoenrich 2018).

In Figure 6, we show theoretical surfaces of section in the vertical phase plane (z, V_z) at six different radii (R = 20, 17, 14, 11, 8, 5 kpc). Stellar orbits in 3D are complex moving over roughly toroidal surfaces about the Galactic Centre (McMillan & Binney 2008). Each panel includes 18 concentric ellipses that correspond to increasing values (the same sequence across all panels) of the vertical action J_z. The central ellipse corresponds to an orbit that is almost circular; for all concentric ellipses, J_R is fixed and J_ϕ is set by the circular orbit at that radius. The area and extent of the outer ellipse at $R = R_\odot$ matches the extent of the signal in Figure 6a. The outer ellipse in all other panels conserves the quantity $2\pi J_z$; the mean radius of each ellipse is proportional to $\sqrt{J_z}$. In Figure 5a, each point in the (z, V_z) plane is characterised by a range of orbital energies; for all J_z, there is a spread in Ω_z because stars have a wide spread in L_z (Binney & Schoenrich 2018).

3.1.2 Spiral unravelled

In Figure 5a, we find the low-order pattern is usefully described by an Archimedean spiral such that, at a given phase angle $\psi_{\rm ps}$,

$$r_{\rm ps} \quad = \quad k(\psi_{\rm ps} + \eta) \qquad (1)$$

where k is a scaling constant and η allows for a fixed pattern to be rotated in the (z, V_z) plane. In our normalized phase space[3], the

[3] The variables $r_{\rm ps}$ and $\psi_{\rm ps}$ are related to $\sqrt{J_z}$ and θ_z respectively; our convention is useful for rescaling the vertical phase plane in different regions

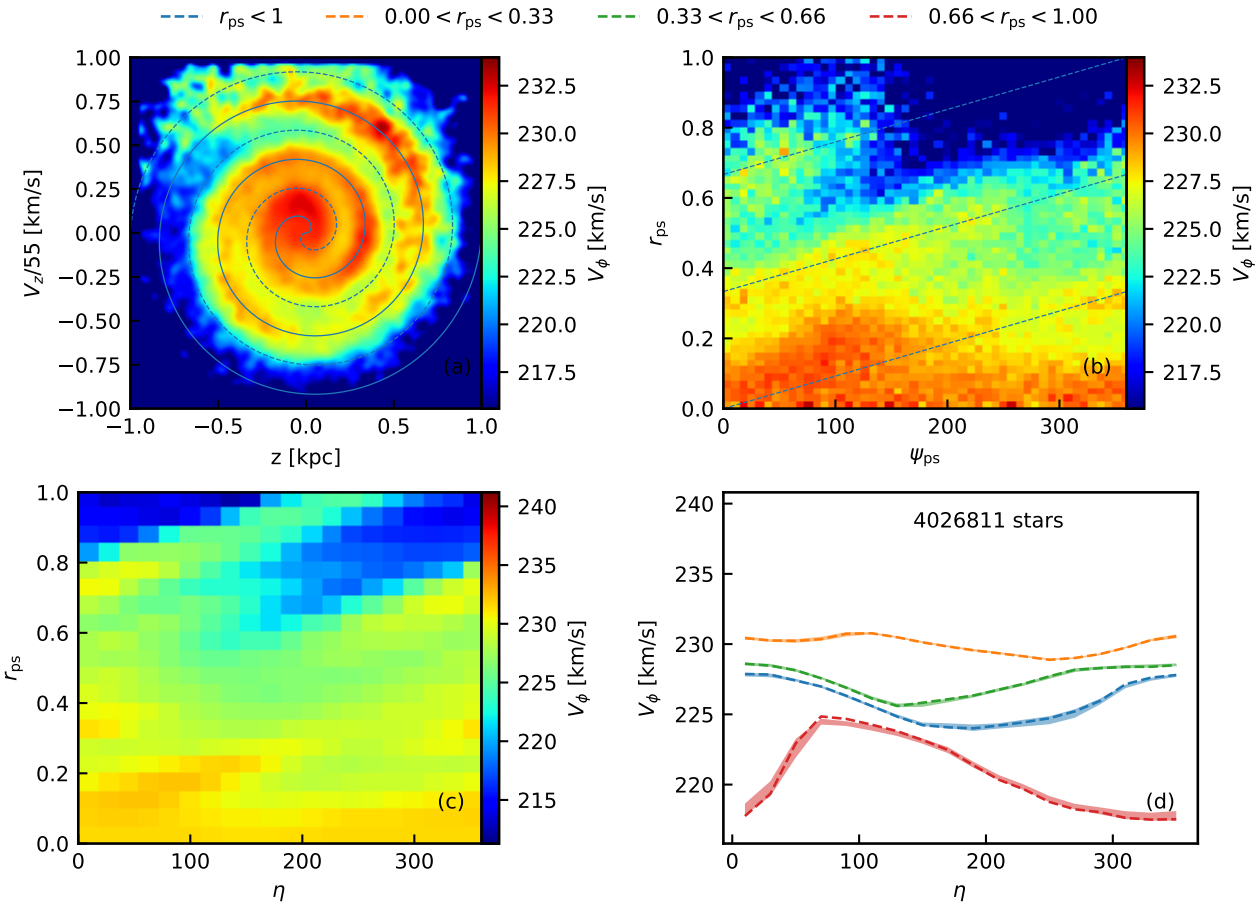

Figure 5. Kinematic properties of stars in the solar neighbourhood using data from *Gaia* DR2. Stars were selected to be within $|R - R_\odot| < 1.0$ kpc and $|\phi - \phi_\odot| < 15°$. (a) Map of $\langle V_\phi(z, V_z)\rangle$, i.e. average azimuthal velocity V_ϕ in (z, V_z) plane. Archimedean spirals are overplotted and defined by $r_{ps} = (\psi_{ps} + \eta)/(6\pi)$ with phase angles $\eta = 0$ (solid) and $\eta = 180°$ (dotted). (b) The unwound spiral pattern as a function of r_{ps} and ψ_{ps}. The three diagonal lines are defined for three different radial ranges in (z, V_z) plane. The colour coding is the volume-weighted median azimuthal velocity at each point in (z, V_z). (c) For a fixed spiral pattern, we can plot the same values as a function of r_{ps} and spiral offset angle η; if the archimedean spiral was a good fit to the spiral phase, the bands would be horizontal because the entire spiral would pass through the peak data in (z, V_z) at the same offset angle η. The diagonal banding indicates the fit is not perfect. (d) Median azimuthal velocity as a function of offset angle η for three radial ranges (orange, green, red) as indicated, and where the blue curve is averaged over all radii. The band shows the 68% confidence zone based on bootstrap samples. A well-defined pattern in the data should produce a peak and a minimum in V_ϕ at distinct η values spaced by 180°. As expected, the blue curve peaks at $\eta \approx 0$ with a minimum near $\eta \approx 180°$; the behaviour of the other curves is less well defined.

radial and angular coordinates are defined as

$$r_{ps} = \sqrt{(V_z/55)^2 + z^2} \quad (2)$$

$$\psi_{ps} = \tan^{-1}(V_z/55, z). \quad (3)$$

The spiral phase manifests as lines or striations in polar coordinates (r_{ps}, ψ_{ps}), and they form straight lines for Archimedean spirals. Figure 5b shows the map of $\langle V_\phi\rangle$ in polar coordinates, and we can see overdensities along lines at specific intervals. The wrapped dashed line corresponds to the case of $\eta = 0$, with angle ψ_{ps} going from 0 to 6π. For $0 < \psi_{ps} < 2\pi$ $(0 < r_{ps} < 0.33)$, the spiral misses the overdensity. For $2\pi < \psi_{ps} < 6\pi$ $(0.33 < r_{ps} < 1.0)$, the spiral traces the overdensity.

Figure 5c presents the median azimuthal velocity as function of r_{ps} for each spiral defined by η. If the system is a perfect Archimedean spiral and the correct scaling k is used, then there should be no pattern of slanted lines in this projection. But we do see weak slanted residuals which indicates that our model is too simplistic. In Figure 5d, the median azimuthal velocity is shown as function of η for three different radial ranges in r_{ps} as indicated. We split the spiral into three zones based on r_{ps}, inner $r_{ps} < 0.33$ (orange), middle $0.33 < r_{ps} < 0.66$ (green) and outer $0.66 < r_{ps} < 1.0$ (red) where the 1σ dispersions are also shown. In addition to the radial intervals, we also show results (blue curve) for the full radial range ($r_{ps} < 1.0$). This is an average over the full spiral phase. As expected, the maximum is at around $\eta = 0$ and minimum is at around $\eta = \pi$. However the radial divisions show the maximum and minimum at different values of η, indicating that the spiral pattern changes slightly with radial distance. These statistical profiles are

of the Galaxy to remove the strong distortion imposed by the underlying potential; see Figure 6. After (Antoja et al. 2018), the spiral phase pattern can be rendered more 'circular' to compare the η offset and amplitude for different parts of the disc more readily.

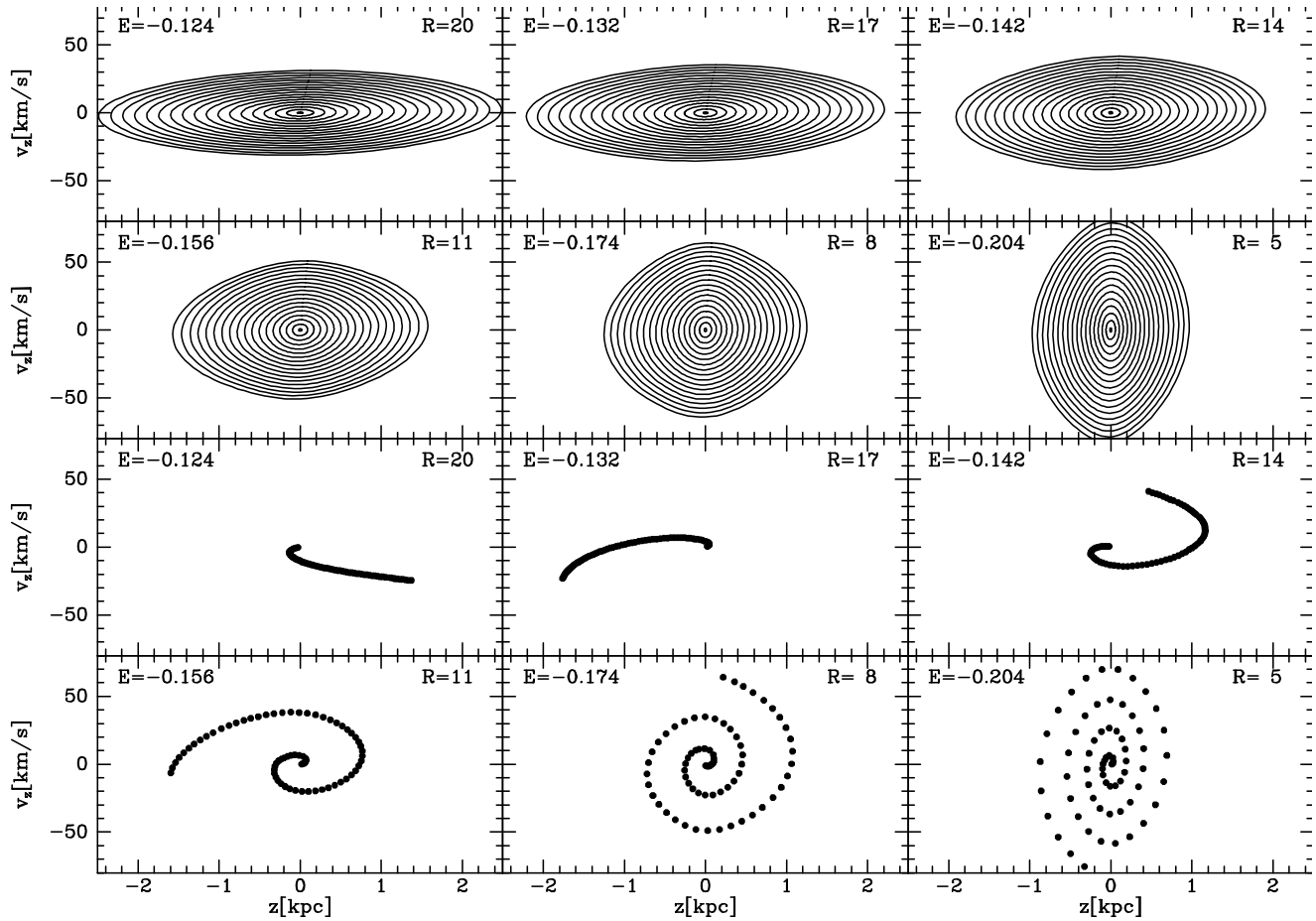

Figure 6. The top 6 panels show surfaces of section in the vertical phase plane (z, V_z) at six different radii (R = 20, 17, 14, 11, 8, 5 kpc) which are chosen to match the radial extent of our new disc simulations and the *Gaia*/GALAH study. The adopted Galactic potential is the prescribed 'best model' from McMillan (2011). Our work is motivated by Antoja's spiral phase pattern at R = 8 kpc: (a) we show only $V_\phi > 0$; (b) the amplitude of the outer ellipse at R = 8 kpc is chosen to match the *Gaia* data; (c) all other outermost ellipses in the other panels conserve the same area (= $2\pi J_z$). For each panel, the orbital energies E are indicated. The J_z values for each concentric ellipse moving outwards are: 0.008, 0.20, 0.65, 1.35, 2.31, 3.52, 4.99, 6.71, 8.69, 10.93, 13.42, 16.17, 19.17, 22.43, 25.94, 29.71, 33.73, 38.01 kpc km s^{-1}. In the outer disc, the ellipses elongate in z because stars travel farther and slower in the weaker disc potential. All orbits have radial action J_R = 0.01 kpc^2 Myr^{-1} = 9.78 kpc km s^{-1} and J_ϕ for the circular orbit at the quoted radius. The bottom 6 panels coincide with the panels above indicated by the total energies; these reveal the impact of phase wrapping after 250 Myr where all points are initially lined up along $\psi_{\rm ps}$ = 1.3 rad. Across the inner disc, the stronger disc gravity leads to faster vertical oscillations which results in stronger phase wrapping.

an important aspect of the analysis because the visual impression of the spiral phase images can be misleading. In this unravelled plane, a well defined spiral segment is revealed as a sine curve over 2π; a bigger amplitude reflects a stronger contrast of the spiral phase over background.

Throughout Figure 5, volume weighting is used. This is essential for our study because the sample is centrally concentrated and the density falls off with $r_{\rm ps}$; number-weighted estimates are highly biased and unrepresentative of the overall spiral pattern. The volume-weighted median is computed as follows. We create a median or average map of $\langle V_\phi(z, V_z/55)\rangle$, and use it generate V_ϕ for any arbitrary position in (z, V_z) space via linear interpolation. Next, we generate points uniformly over a circle in $(z, V_z/55)$ space and assign $(r_{\rm ps}, \eta)$ for each generated point using,

$$\eta \quad = \quad \mathrm{mod}(r_{\rm ps}/k - \psi_{\rm ps}, 2\pi), \qquad (4)$$

i.e., we associate each point with a spiral. By binning the points in η, we compute volume-weighted quantities like median V_ϕ for each spiral.

3.1.3 *Dependence of spiral phase on location*

Figure 7 explores how the properties of the spiral phase vary with location in the Galaxy. The top row (a-c) incorporates the exact data used by Antoja et al. (2018), which is very local to the Sun. The second row (d-f) is the expanded sample as studied in Figure 5 centered on the Sun. The volume of the latter sample is twenty times larger than the former, yet the spiral pattern remains essentially the same. The remaining panels use the larger volume. As illustrated in Figure 1, the third row (g-i) examines a sample centered at $R = R_\odot + 0.5$ kpc, while the fourth row (j-l) explores a sample centered at $R = R_\odot - 0.5$ kpc; the spiral pattern is evident. Once again, we split the spiral phase into three zones based on $r_{\rm ps}$ and where the blue curve is averaged over the full domain. For each curve, the difference between the maximum and minimum value of V_ϕ indicates the relative strength of the spiral.

The remaining panels examines samples in neighbouring spheres close to the solar neighbourhood, two offset to larger and smaller radii, and two offset in both directions in azimuth. The

fifth row (m-o) explores a sample with Galactocentric longitude $|\phi - (\phi_\odot + 7.5^\circ)| \leqslant 7.5^\circ$, while the sixth row (p-r) explores a sample with $|\phi - (\phi_\odot - 7.5^\circ)| \leqslant 7.5^\circ$. In the radial direction, the samples span $|R - R_\odot| \leqslant 1$ kpc. As seen from the right-hand column, their spiral phase patterns (o,r) are similar and much the same as seen in the second row (f) for the large local volume.

Near the origin in (z, V_z), there is a clear difference in the η offset of the spiral phase when we compare the inner disc (g) and outer disc (j) which is *not* seen when we move in azimuth to higher (m) and lower (p) values of ϕ. The outer disc appears more unravelled, entirely as anticipated from theory (Figure 6). As shown by the curves, for the inner disc, the mid-zone spiral (i) is strong while the outer-zone spiral is weak. For the outer disc (l), the opposite effect is seen. As we discuss below with the GALAH data, where a related effect is seen in metallicity due to its radial trend, this is consistent with our sketch in Figure 1. The thin to thick disc transition shown here was first presented by Hayden et al. (2015) from the APOGEE survey who found that the thick disc peters out near the Solar Circle. They find elevated thin disc stars beyond here presumably because the disc becomes flared or warped, or both (Schönrich & Dehnen 2018).

We also inspected the 2-kpc diameter volume centred at $R = R_\odot \pm 1$ kpc; the spiral phase was evident but less well defined due to the smaller number of stars and the larger cumulative errors on measured parameters. *The spiral phase pattern is clearly a disc-wide phenomenon.*

3.2 GALAH analysis

In Figure 9, we explore whether the properties of the spiral phase evolves with the stellar abundances taken from the GALAH survey. We use $[\alpha/\mathrm{Fe}]$ to separate stars into thick (a-c) and thin disc (b-d) populations (cf. Adibekyan et al. 2012) as illustrated in Figure 2. Additionally, we subdivide the thin disc into 4 metallicity bins as indicated and study them individually. The thick disc (a) shows only weak evidence for the spiral phase structure as compared to the thin disc (b). However, the thick disc sample is a factor of 9 smaller than the thin disc sample.

The remaining panels in Figure 9 show the metallicity splits for the thin disc. *A clear trend with metallicity can be seen*. The outer spiral zone is strongest for the most metal poor stars (g) and becomes weaker as we increase the metallicity of the sample (j,m,p). With reference to Figure 3: GALAH stars with $|V_z| > 40$ km s^{-1} are overwhelmingly metal poor and so the outer spiral is much stronger here. The contrast is clear in (i) from the clean red sine curve compared with the flat green curve, i.e. the mid zone is weakest for metal poor stars and becomes stronger as we increase the metallicity of the subsample. With our radial cut, $|R - R_\odot| \leqslant 1$ kpc, relatively metal rich stars in the sample will have a mean radius less than $R_\odot$ and metal poor stars will have a mean radius greater than $R_\odot$. (A related metallicity effect is observed in Figure 7 where we varied the radial distance R of the sample. The spiral contrast in the outer zone becomes stronger as we move outwards in R and the mid zone becomes stronger as we move inwards in R.)

We also looked at the different metallicity splits (not shown here) but this time keeping the sample size the same for all of them (i.e. 31666 stars each from random sampling). The spiral contrast in the thin disc and for the metallicity splits is reduced but with higher contrast than the thick disc. This suggests that the spiral pattern in the thick disc may be intrinsically weaker than for the colder thin disc. For the metal poor *thin* disc, a pattern in the outermost zone can be seen, and for the metal rich *thin* disc, the spiral phase in the mid zone is quite clear. The observed trends are consistent with the negative metallicity gradient with increasing R and z.

The trend in the spiral pattern with metallicity is smoothly varying with no evidence for a chemically homogeneous or single age population (e.g. star cluster) dominating the spiral phase at fixed V_ϕ. To explore this further, we need either a large sample of metal poor and metal rich stars in a limited range in R, or a large sample of stars at $R_\odot \pm 0.5$ kpc but within a small range in [Fe/H].

3.3 LAMOST analysis

To stress the robustness of the spiral phase signature, we show that it can be extracted from the LAMOST survey (Deng et al. 2012). LAMOST (Large Sky Area Multi-object Survey Telescope), based in Hibei Province in China, is a lower spectral resolution ($R \sim 1800$) survey but has observed a far greater number of stars than other ground-based surveys, with over 1.5 million stellar spectra collected to date. The third data release (LAMOST DR3) is available at https://dr3.lamost.org and can be accessed over the same volume as the GALAH survey. The database does not supply $[\alpha/\mathrm{Fe}]$ ratios so we are unable to separate the thin and thick discs. But we note the survey is overwhelmed by thin disk stars so that the $V_\phi(z, V_z)$ results presented in Figure 10 are best compared to the GALAH data for the thin disk (Figure 9). We note two things: (i) a weak spiral phase is evident, and (ii) the results resemble the GALAH thin disk results.

4 ACTIONS

The unique ability of *Gaia* to supply 6D phase space motions for millions of stars allows us to divide the stars into different action domains. We use `galpy` (Bovy 2015) and our Galactic parameters (Section 2.1) to compute J_R, J_ϕ (L_z) and J_z for all stars that overlap between GALAH and *Gaia*. In Figure 4, for ease of presentation, we normalised the action units (km s^{-1} kpc) to the product $R_\odot v_\odot$ and logged the data for J_R and J_ϕ. In Figure 8, we discuss these results in terms of the vertical phase plane. In the top two rows, for the median value over the *Gaia* volume, $\hat{J_R} = 0.01$, we divide stars into more elliptic (a) and more circular (d) orbits. Note the remarkably strong spiral phase that can be traced to the centre in the case of more circular orbits, confirmed by the orange sine curve in (f). *This is the clearest manifestation to date that the spiral phase can be traced to the origin of the vertical phase plane.*

The next four rows arise from subdividing along another action, L_z (J_ϕ), into high (g,m) and low (j,p) angular momentum sets. For flat rotation, this directly relates the guiding radius R_g of the oscillating orbit in the plane. On average, stars with $L_z > 1$ come from outside the Sun's orbit, and stars with $L_z < 1$ from inside. We now observe in (p) that the tight inner spiral comes from more circular orbits for stars whose guiding radius lies inside of the Sun's orbit where the radial excursions (apogalacticon) reach the Solar neighbourhood. Note also that the clean spiral in (j) has a different η offset from (p) reflecting the larger guiding radius of these stars (see Figure 6). When the radial action is large, a broader set of orbits is moving through the Antoja volume, thereby washing out the coherence of the spiral phase.

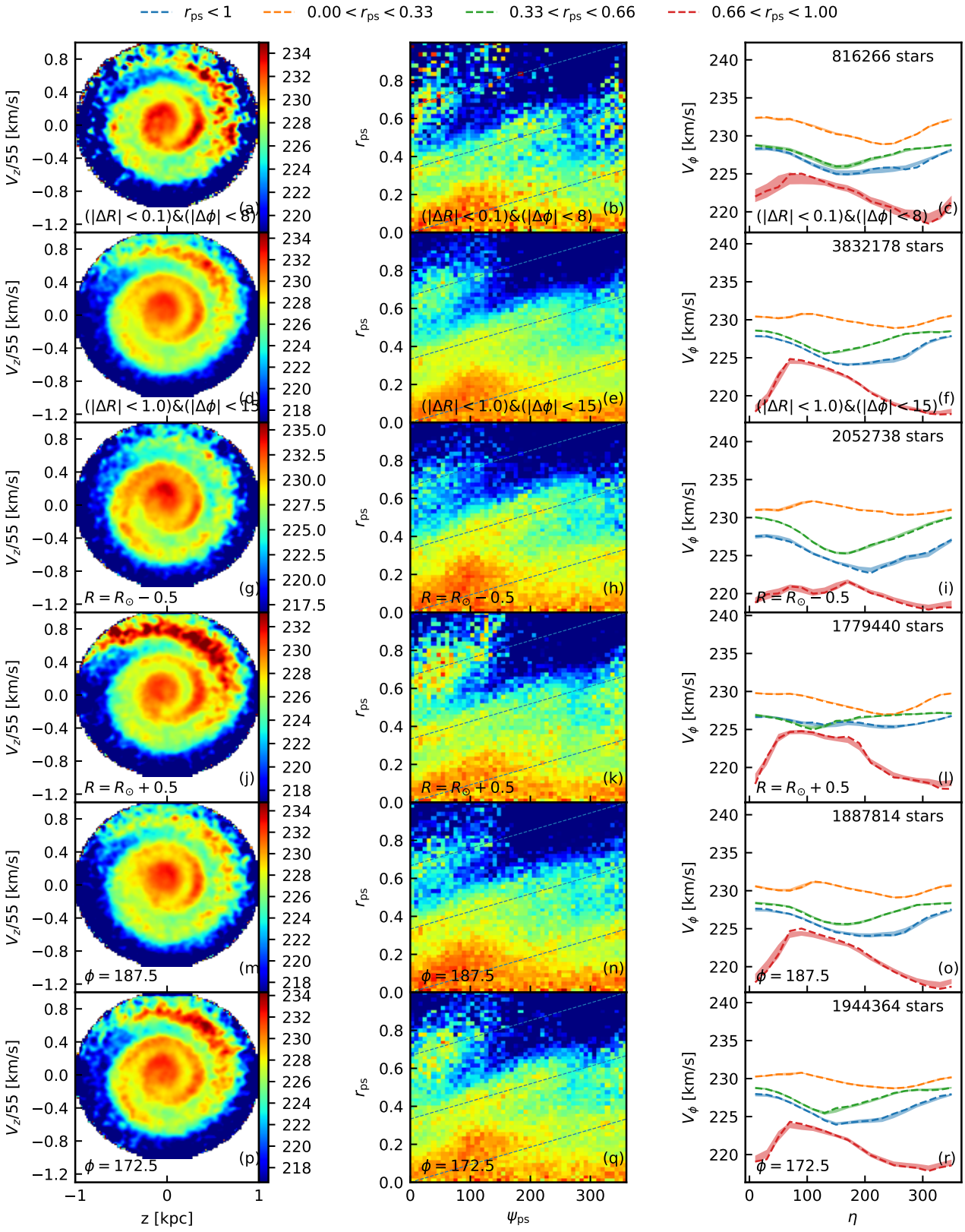

Figure 7. Kinematic properties of stars in the solar neighbourhood using data from *Gaia* DR2. Each row corresponds to different selections of stars. (a,b,c) Stars with $|R - R_\odot| < 0.1$ kpc and $|\phi - \phi_\odot| < 7.5°$. (d,e,f) Stars with $|R - R_\odot| < 1.0$ kpc and $|\phi - \phi_\odot| < 15°$. (g,h,i) Stars with $(|R - (R_\odot - 0.5)| < 1.0$ kpc and $|\phi - \phi_\odot| < 15°$. (j,k,l) Stars with $|R - (R_\odot + 0.5)| < 1.0$ kpc and $|\phi - \phi_\odot| < 15°$. (m,n,o) Stars with $|R - R_\odot| < 1.0$ kpc and $|\phi - (\phi_\odot + 7.5°)| < 7.5°$. (p,q,r) Stars with $|R - R_\odot| < 1.0$ kpc and $|\phi - (\phi_\odot - 7.5°)| < 7.5°$. Panels in the left column show the azimuthal velocity in (z, V_z) plane. The panels in middle column show the azimuthal velocity in polar coordinates (r_{ps}, ψ_{ps}) in phase space. The panels in the right column show the volume-weighted median azimuthal velocity for all phase angles η.

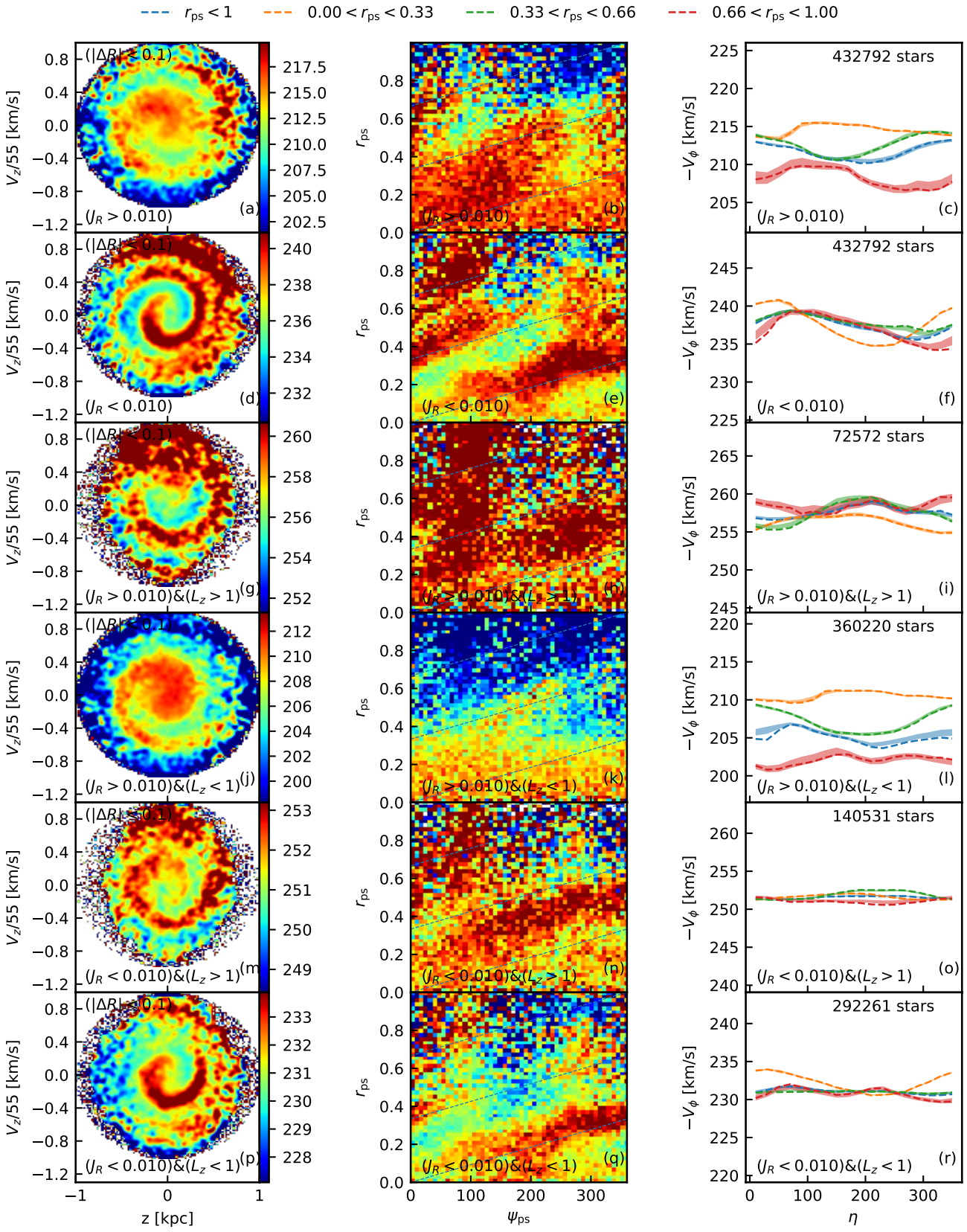

Figure 8. An analysis of actions ($J_R, J_\phi = L_z$) over the original Antoja volume ($|\Delta R| < 0.1$ kpc). The first two rows correspond to stars with $J_R > \hat{J}_R$, the median value, and $J_R < \hat{J}_R$ respectively. The columns are defined in the previous figure. In the second row, more circular orbits passing through the solar neighbourhood carry the spiral phase signal all the way to the origin in (z, V_z), the clearest manifestation of this inner signature to date. The next four rows divide the domain further in terms of high and low L_z, i.e. $J_R > \hat{J}_R$, $L_z > 1$ (row 3); $J_R > \hat{J}_R$, $L_z < 1$ (row 4); $J_R < \hat{J}_R$, $L_z > 1$ (row 5); $J_R < \hat{J}_R$, $L_z < 1$ (row 6). The last row reveals the tight inner spiral arises from stars with guiding radii inside $R_\odot$ that reach apogalacticon in the solar neighbourhood.

5 VELOCITY ELLIPSOID

Unlike particle motions in a gas, the stellar velocity dispersion tensor for a disc galaxy is far from isotropic (Binney & Tremaine 2008). The orientation of the long axis of the velocity ellipsoid depends on the shape of the Galactic potential and the local phase space distribution function (Lynden-Bell 1962; Ollongren 1962; Hori & Liu 1963). Coupling between the vertical and radial oscillations leads to a tilt α_T of the velocity ellipsoid with respect to the Galactic plane, such that

$$\tan(2\,\alpha_T) \quad = \quad \frac{2\,\overline{V_R V_z}}{\sigma_R^2 - \sigma_z^2} \qquad (5)$$

where σ_R and σ_z are the radial and vertical stellar dispersions[4]. Their in-plane ratio ($\sigma_z/\sigma_R \approx 0.6$) is set largely by κ/Ω where κ is the local epicyclic frequency and Ω is the angular frequency of a local circular orbit (Ida et al. 1993). The averaged product $\overline{V_R V_z}$ is an observed quantity that can be derived in localised regions of the disc or halo (Binney et al. 2014). It features in the axisymmetric Jeans equation

$$\frac{1}{R}\frac{\partial}{\partial R}(R\rho_\star \overline{V_R V_z}) + \frac{\partial}{\partial z}(\rho_\star \sigma_z^2) + \rho_\star \frac{\partial \Phi}{\partial z} \quad = \quad 0 \qquad (6)$$

where $(\Phi, \rho_\star)$ are the local gravitational potential and mass density pair. We note that it is not possible to derive $(\Phi, \rho_\star)$ from the tilt distribution alone except for one idealized case (Binney & McMillan 2011).

In their study of the RAVE survey, Siebert et al. (2008) find a velocity ellipsoid tilt of $\alpha_T = 7.1^\circ \pm 1.8^\circ$ at 1 kpc above the Sun's position pointing at the Galactic Centre, confirmed by Carollo et al. (2010). Both studies find the signal is relatively insensitive to contamination by foreground stars and substructure. Büdenbender et al. (2015) extend the measurement of tilt to $|z| \approx 2.5$ kpc. As expected, α_T increases with height in order to keep the long axis of the velocity ellipsoid pointing at the Galactic Centre (Binney et al. 2014). Here, within our 2-kpc diameter sphere, we find a strong footprint of this signal within the *Gaia* DR2 observations. By symmetry, the ellipsoidal tilt is mirrored above and below the disc. We summarize the main result below; a more detailed analysis is to follow.

5.1 *Gaia* analysis

Figure 11 was first presented by Antoja et al. (2018), but we revisit the $\langle V_R(z, V_z)\rangle$ distribution because an important observation has been overlooked. The volume considered is indicated once again as the narrow ellipse in Figure 1. As noted by the *Gaia* team, a weak spiral phase is evident. But underlying the phase pattern is a well defined quadrupole ($\mp\pm$) pattern not commented on to date.

This is arguably the clearest signature to date of the tilt of the velocity ellipsoid far from the plane. In Figure 13, we illustrate how this pattern arises. Consider a cylinder perpendicular the disc that encompasses the solar neighbourhood. Now consider a velocity ellipsoid with a long axis defined by stars that stream in both directions. As we look upwards, we observe the component of the streaming motion that projects $+V_R$ along the $+z$ axis, and $-V_R$ along the $-z$ axis. The exact opposite is true if we observe downwards. This gives rise to the quadrupole pattern in $\langle V_R(z, V_z)\rangle$.

[4] Equation 1 in Siebert et al. (2008) contains a typographical error: the minus sign is missing between the squared terms in the denominator.

5.2 GALAH analysis

In Figure 12, we present the phase space distribution weighted by the radial velocity, $\langle V_R(z, V_z)\rangle$ specifically for the GALAH survey over the same volume used for the construction of $\langle V_\phi(z, V_z)\rangle$. It is noticeable that the spiral phase pattern is relatively weak in all panels but seen most clearly in the summed thin disc panel (b). In all thin disc panels, we do see the distinctive quadrupole pattern, identified in the previous section arising from the tilt of the velocity ellipsoid. The existence of the spiral phase in both $\langle V_\phi(z, V_z)\rangle$ and $\langle V_R(z, V_z)\rangle$ has implications for disc dynamics. We now investigate with dynamical simulations what one can learn from the new data.

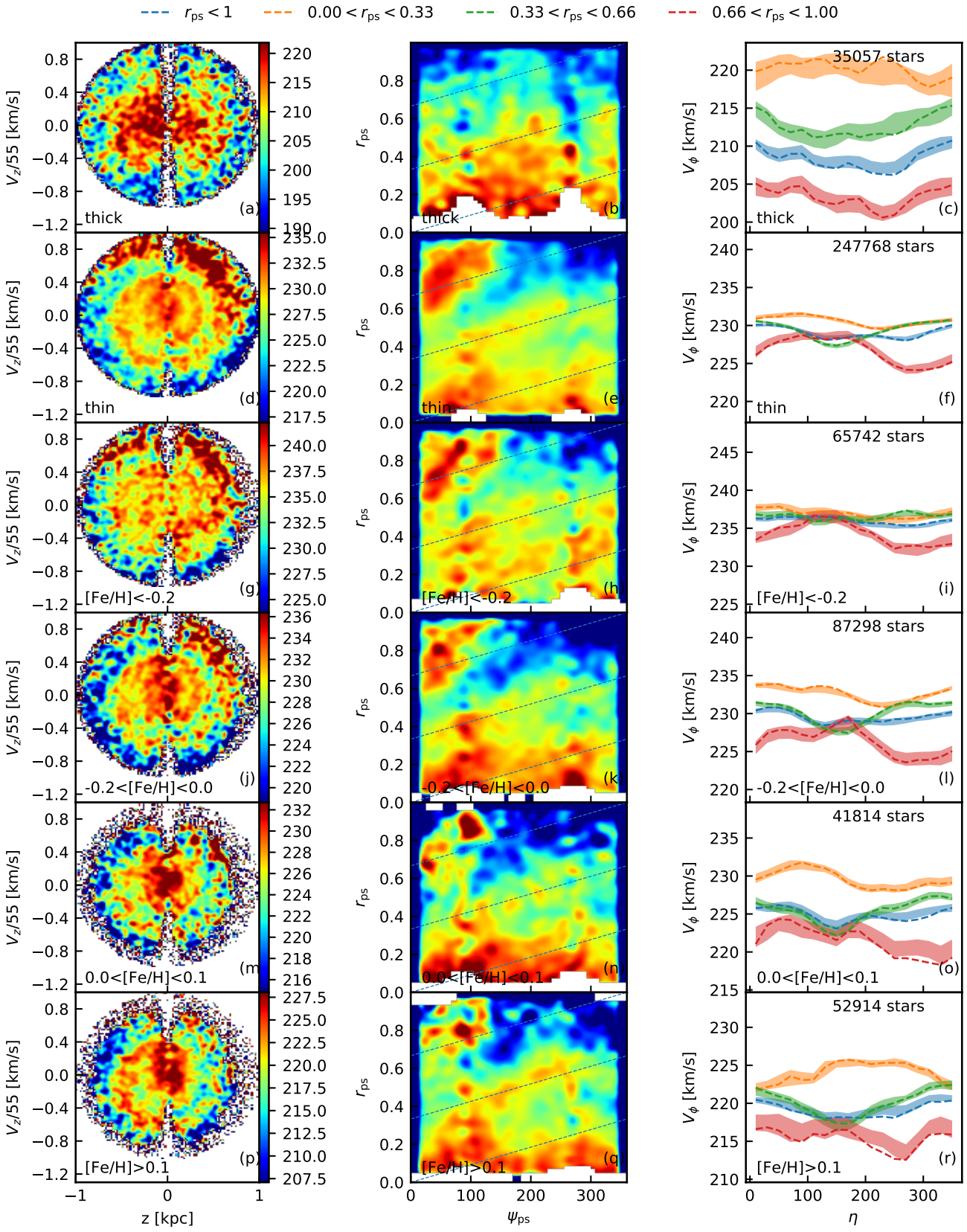

Figure 9. Kinematic properties of stars in the solar neighborhood using data from GALAH and Gaia DR2. The panel definitions are same as in Figure 7. Each row corresponds to a different selection of stars based on elemental abundances. (a,b,c) Thick disc stars identified with $[\alpha/\mathrm{Fe}] > 0.15$. (d,e,f) Thin disc stars identified with $[\alpha/\mathrm{Fe}] < 0.15$. (g,h,i) Thin disc stars with $[\mathrm{Fe/H}] < -0.2$. (j,k,l) Thin disc stars with $-0.2 < [\mathrm{Fe/H}] < 0.0$. (m,n,o) Thin disc stars with $0.0 < [\mathrm{Fe/H}] < 0.1$. (p,q,r) Thin disc stars with $[\mathrm{Fe/H}] > 0.1$.

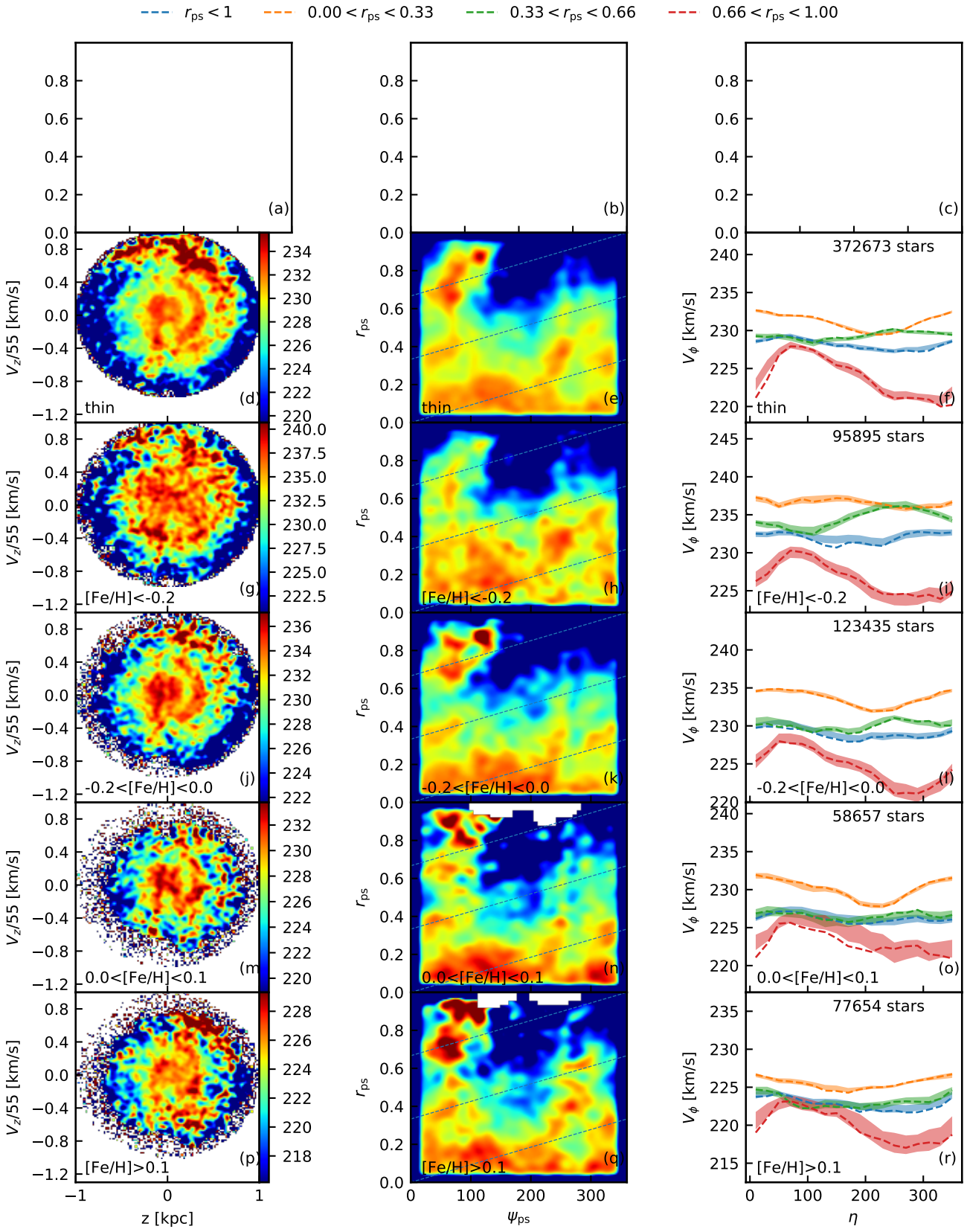

Figure 10. Kinematic properties of stars in the solar neighborhood using data from LAMOST DR3 and Gaia DR2. The panel definitions are the same as in Figure 9. We do not have [α/Fe] estimates for LAMOST stars, so we leave the top panels empty because stars cannot be split into thin and thick disc components.

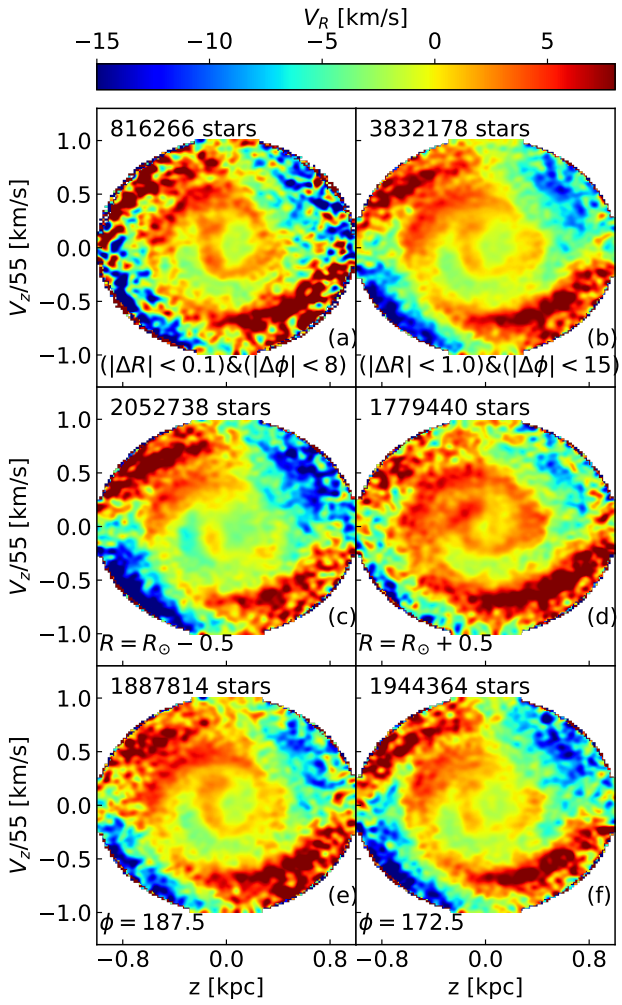

Figure 11. Map of median V_R in (z, V_z) plane for stars in the solar neighborhood using data from Gaia DR2. The sample definitions are same as in Figure 7. The quadrupole defined by the sign changes in each quadrant are due to the tilt of the velocity ellipsoid (see the sketch in Figure 13). Note that a weak spiral phase pattern is visible in the center. The pattern is stronger for the $R = R_\odot - 0.5$ case as compared to $R = R_\odot + 0.5$ case.

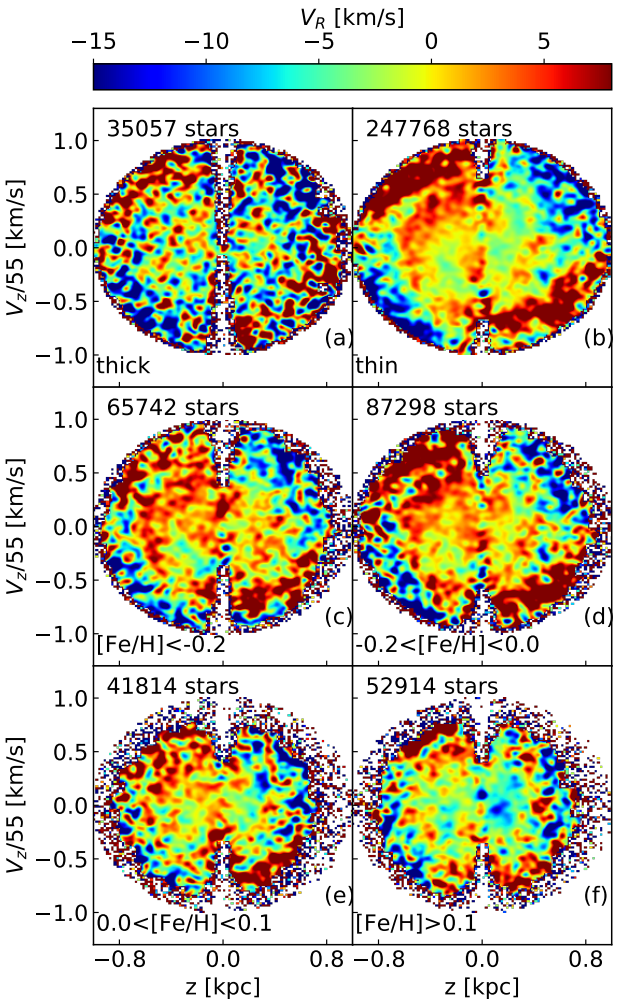

Figure 12. Map of median V_R in (z, V_z) plane for stars in the solar neighborhood using data from GALAH and Gaia DR2. The sample definitions are the same as in Figure 9.

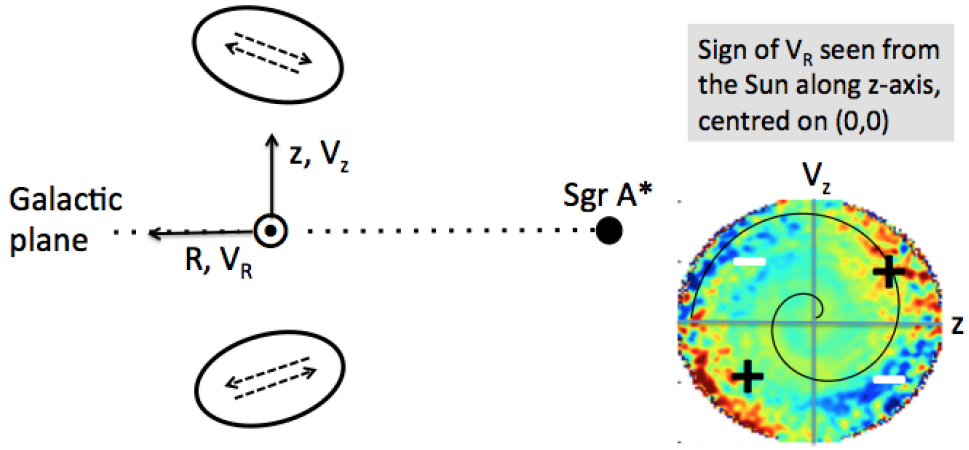

Figure 13. (Left) The adopted coordinate frame in phase space defined with respect to the Galactic cylindrical coordinates shown with respect to the Sun's position. The tilted velocity ellipsoids above and below the Galactic plane are also indicated. The dashed arrows show the direction of the fastest motions within the ellipsoid. (Right) When viewed from the Sun, the tilted velocity ellipsoids produce a characteristic quadrupole $\mp\pm$ pattern as seen in the GALAH and *Gaia* data. The data are taken from Figure 11; see the text for further discussion.

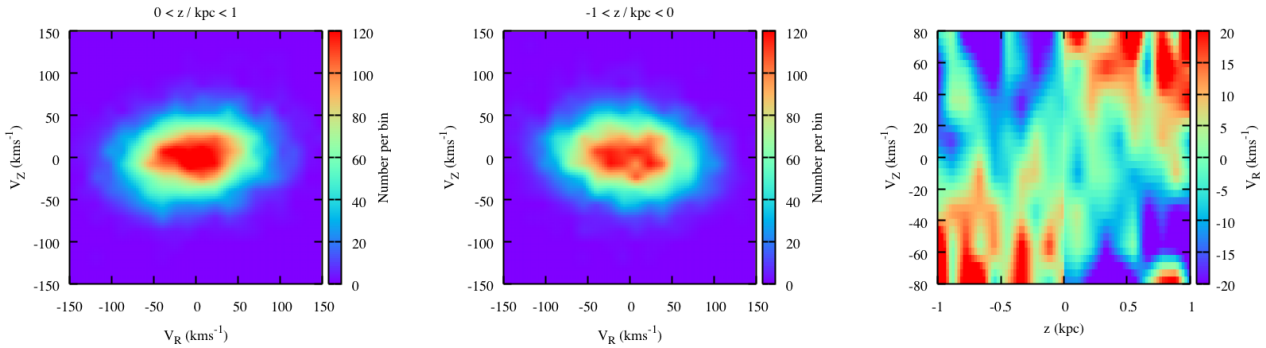

Figure 14. Velocity ellipsoid for star particles in the unperturbed Galaxy model above (left) and below (centre) the disc plane. The right panel shows the phase space distribution $\langle V_R(z, V_z)\rangle$ corresponding to the panels to the left. Compare these figures with Figure 13. Note that the tilt of the ellipsoid in each case here is mirrored with respect to the vertical axis compared to the corresponding ellispsoid in Figure 13 because the $R - z$ reference system (implicit in the left and central panels) is mirrored in the same way.

6 DYNAMICAL IMPLICATIONS

6.1 Amplitude of the spiral phase

Antoja et al. (2018) present a simple model for the spiral phase in terms of the settling action of the Galactic disc after it has been hit by the transiting Sgr dwarf. Following Candlish et al. (2014), they carry out at a perturbation analysis using a Miyamoto & Nagai (1975) disc and find that a transit occurred in the past 350 Myr to 850 Myr. We believe this model to be an incomplete description of what is needed to understand the spiral phase pattern and its implications. The additional considerations are: (i) the amplitudes $|z_{\rm max}|$, $|V_{z_{\rm max}}|$ of the response in the (z, V_z) plane, and their ratio ($\mathcal{A}_z = |z_{\rm max}|/|V_{z_{\rm max}}|$), are strongly dependent on a star's location in the disc and Sgr's orbit and mass; (ii) Sgr is quasi-impulsive (Binney & Schoenrich 2018) but also induces a forced oscillation because of its grazing incidence and low-flying orbit over the plane; (iii) Sgr performs multiple disc crossings which messes up the phase coherence imposed by the last transit. All of these factors must be considered in the final analysis if we are to provide a dynamical age for the Antoja spiral.

On the first point, in Figure 6, we illustrate the phase-space amplitude response of the disc using a Galactic mass model, specifically the 'best model' taken from McMillan (2011). The top six panels reveal that the total amplitudes in the (z,V_z) plane, i.e. $|z_{\rm max}|$, $|V_{z_{\rm max}}|$, and their ratio $\mathcal{A}_z$, are a strong function of Galactocentric radius R. Thus, in Section 2, we normalise both axes using ($|z_{\rm max}| = 1$ kpc, $|V_{z_{\rm max}}| = 55$ km s^{-1}) to match the circular outer envelope used by Antoja et al. (2018) for the spiral pattern at $R = 8$ kpc.

The bottom six panels of Figure 6 illustrate the impact of phase wrapping as a function of R. In terms of the elevation of stars above the disc, the spiral phase is expected to be strongest in the outer disc as the new simulations confirm in Section 6. Here the longer dynamical timescales lead to incomplete phase mixing. The spirality becomes evident when we normalise the phase-space axes to correct for the strong amplitude ratio ($\mathcal{A}_z$) dependence with radius R (cf. Section 2).

In what follows (Section 6.2), the dynamics of tides shed light on the perturber/disc interaction. These equations can be normalised directly from realistic N-body simulations (e.g. Salo & Laurikainen 2000). More usefully, in Section 6, we need numerical simulations to determine how the phase space amplitude $\mathcal{A}_z$, and the coherence or contrast of the spiral phase, depend on the perturber's orbit and passage of time since the last disc crossing.

6.2 Impulse approximation

When a satellite mass passes close to a self-gravitating disc, each Fourier component m of the impulsive perturber potential $\Phi_{\rm P}$ will generates its own signature in the disc (Terquem 1998; Salo & Laurikainen 2000; Bovy 2015). The total potential felt by a disc particle is

$$\Phi_{\rm tot}(R, \phi, z) \quad = \quad \Phi_{\rm MW} + \Phi_{\rm P}(1 + \frac{z}{D}\sin i)\cos(m\phi) \qquad (7)$$

where $\Phi_{\rm P} \sim GM_{\rm P}R/D^2$ is the approximate potential of the perturber and $\Phi_{\rm MW}$ describes the disc+bulge+halo contribution from the Galaxy. The term $\sin i$ corrects for the orbit inclination of the perturber, and the expression is valid for $z/D \ll 1$ and $R/D \ll 1$.

In all likelihood, the story is more complicated because (a) the perturber can be heavily distorted by the underlying galaxy, (b) the applied force may not be impulsive, and (c) the disc response in detail depends on the disc properties (e.g. vertical structure). Indeed, models consistently show that Sgr originally transited the disc perpendicular to the plane. But the last transit was at a glancing angle ($i \lesssim 30^\circ$) of the Galactic plane and Sgr is now orbiting within 10−20 kpc of the disc plane (Law et al. 2005; Tepper-García & Bland-Hawthorn 2018). Given the orbit details, the simulations presented in Section 6 suggest that the force imposed by Sgr is not especially impulsive. Binney & Schoenrich (2018) have used the impulse approximation to show how oscillations in the different phase planes become coupled. In a follow-up paper, we find the application of action and modal analysis to both simulations and data to be highly instructive.

6.3 Forced oscillator approximation

When the disc-crossing time τ_C of the perturber is comparable to the period of the oscillating stars, the stars is said to be 'driven' as a forced oscillator. Then the total potential felt by a disc particle is

$$\Phi_{\rm tot}(R, \phi, z) \quad = \quad \Phi_{\rm MW} + \Phi_{\rm FO} \qquad (8)$$

where

$$\Phi_{\rm FO} \quad = \quad \Phi_{\rm P}(1 + \frac{z}{D}\sin i)\cos m(\phi - \Omega_o t) \qquad (9)$$

where Ω_o is the projected orbital frequency of the perturber in the disc plane. The vertical response of a particle is given by

$$\frac{d^2 z_m}{dt^2} \quad = \quad -\omega_o^2 z_m + \frac{d\Phi_{\rm P}}{dz} \qquad (10)$$

where ω_o is the vertical frequency of a star in the unperturbed Galactic potential, i.e.

$$\omega_o^2 \quad = \quad \frac{1}{z}\frac{d\Phi_{\rm MW}}{dz}. \qquad (11)$$

After applying Poisson's equation and the continuity equation connecting the perturbed density with the perturbed potential, the general solution is

$$z_m \quad = \quad F(R)\cos(m\Omega_o t) \qquad (12)$$

$$V_{z,m} \quad = \quad -m\Omega_o F(R)\sin(m\Omega_o t) \qquad (13)$$

where

$$F(R) \quad = \quad \frac{1}{\omega_o^2 - \Omega_o^2}\frac{d\Phi_{\rm FO}}{dz}. \qquad (14)$$

Complex solutions exist for the perturbed potential as a function of m, Ω_o, D, R, ϕ and z, but they require numerical integration (Saha & Jog 2006). In the companion paper (Tepper-García et al. 2019), by comparing our hyperbolic and realistic impactor orbits, we analyse the amplitudes and phases of the Fourier terms to demonstrate how the forced oscillation leads to the propagation of waves and a complex interplay between the perturber and the Galaxy. The inner disc is less responsive because the increased self-gravity resists the imposed (perturbed) potential. We find that numerical simulations are important to explore the interaction, supported by theory (Binney & Schoenrich 2018), because the details of the disc response, e.g. the radius for the onset of any corrugation or warp, are strongly dependent on the disc's vertical structure and the impactor orbit properties.

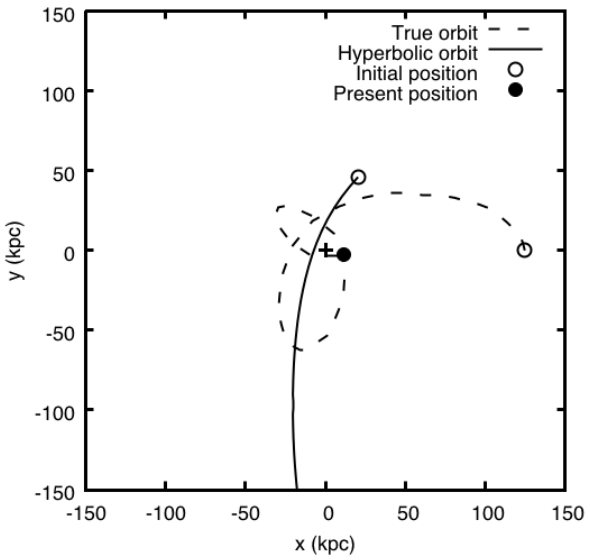

Figure 15. The projection of the polar orbits for the impactors with different mass (hyperbolic vs. realistic) into the (X, Y) plane seen from the NGP. The cross indicates the Galactic Centre. The dashed line shows the complex 'trefoil' orbit of Sgr over the past 2.3 Gyr, now accepted across many studies since Law et al. (2005). Sgr (shown as a filled circle) is due to transit the disc again in about 50 Myr.

7 DYNAMICAL SIMULATIONS

7.1 Set up

In a recent paper (Tepper-García & Bland-Hawthorn 2018), we examine the impact of Sgr on the Galaxy with an N-body, hydrodynamical simulation which has the unique feature of including a gas component demanded by the resolved star-formation history of the dwarf. This work emphasized that the number of disc crossings and the timing of Sgr's orbit are dependent on the rate of mass (dark matter+baryons) loss. We re-run these models without the gas component using an updated Galaxy model (Table 1) over a larger impactor mass and orbit parameter space (Table 2). We include impactors crossing the disc along (unrealistic) hyperbolic orbits to compare single with multiple crossings. The face-on projection of both orbits is shown in Figure 15. This emphasizes the impact of successive crossings on the coherence and longevity of the spiral phase pattern.

The initial conditions of the Galaxy (particle positions, velocities) are constructed following the approach developed by Springel et al. (2005) as implemented in the DICE code (Perret et al. 2014). This relies on the local Maxwellian approximation (Hernquist 1993) to calculate particle velocities, which may not be fully adequate to model N-body systems in strict dynamic equilibrium, particularly dwarf systems (Kazantzidis et al. 2004). This is, however, of no concern in our case since we let the system evolve into a self-consistent configuration before performing our analysis. Our approach also makes use of the epicyclic approximation that relates the azimuthal velocity dispersion to the radial velocity dispersion through the epicycle frequency and the circular frequency.

The Galaxy is modelled as an axisymmetric system, i.e. we assume that the corresponding distribution function is a function of the total energy (E) and the component of the angular momentum projected along the spin axis (L_z) only. In this case, it follows from the axisymmetric Jeans (1915) equation that the mixed moments of the distribution all vanish, i.e. $\langle \sigma_R \sigma_z \rangle \equiv 0$, and that the radial and vertical velocity dispersions are equal everywhere, $\sigma_R = \sigma_z$. The latter implies that the projection of the velocity ellipsoid onto the $V_z - V_R$ plane is circular. The former implies a vanishing tilt for the velocity ellipsoid everywhere. However, to ensure the stability of the stellar disc, we adjust σ_R such that[5] Toomre (1964)'s stability parameter $Q_\star \equiv (\sigma_R \kappa / 3.36 G \Sigma_\star) > 1.5$ everywhere. Here κ and $\Sigma_\star$ are the epicyclic frequency and the stellar surface density, respectively. This results in $\sigma_R \neq \sigma_z$, in general. It is important to mention that the condition $Q_\star > 1$ does not ensure stability generally (Zasov & Zaitseva 2017), but it does suffice in our case.

We calculate the time evolution of the composite system representing the Galaxy with their collisionless and gaseous components by solving the Vlasov-Poisson and Euler equations with the N-body adaptive mesh refinement (AMR), gravito-hydrodynamics code RAMSES (version 3.0 of the code described by Teyssier 2002).[6] The contribution of all components to the overall gravitational field is taken into account at all times. The Galaxy model is evolved for roughly 4 Gyr in order to allow the system to settle into a stationary state. We refer to this as the 'unperturbed' model (Model P).

To look for a phase-wrapped signal, in view of Antoja et al. (2018), we consider a model of the Galaxy that has interacted with Sgr. In brief, we model the infall of Sgr using impactors with three different masses (Table 2) using a "single transit" hyperbolic orbit and high-mass impactor using a more realistic orbit with multiple crossings. In our analysis below, we have sampled the simulation in a manner equivalent to the *Gaia* and GALAH analysis.

The relevant subset of configuration space and phase space movies are available at `http://www.physics.usyd.edu.au/~tepper/proj_galah_paper.html`. We present interaction models for a hyperbolic orbit impactor with low (Model T), intermediate (Model S) and high mass (Model R). These are DM-dominated, spheroidal stellar systems that are placed on a hyperbolic orbit with an eccentricity $e = 1.3$ at an initial distance of $D = 50$ kpc and a pericentric radius of $R = 10$ kpc. In the more realistic simulation (Model K), Sgr's first pericentric passage occurred ~ 2.5 Gyr ago, the next one at ~ 1 Gyr ago, and a third one just a few hundred Myr ago, consistent with observations (Ibata et al. 1997). We refer the reader to Tepper-García & Bland-Hawthorn (2018) for more details.

7.2 Reference model: isolated Galaxy

In movie P1,[7] we witness the long-term evolution of the isolated Galaxy model (Model P) summarised in Table 1. The frames are shown with time steps of $\Delta t = 10$ Myr which is short enough to trace most stellar orbits reliably. The disc settles to an equilibrium configuration within a few hundred Myr. This can be seen from the settling to a cold, thin disc in the edge-on and face-on projections, with a constant vertical scaleheight. The disc generates low-level flocculent spiral perturbations consistent with the intrinsic numerical and spatial resolution, but individual stellar orbits confirm that

[5] This adjustment is performed only *after* the azimuthal velocity dispersion is calculated using the epicycle approximation.

[6] We practice an open policy on set-up files for all of our N-body + MHD studies to encourage cross checking and, while this is not a common practice, we strongly encourage others to do the same. All files are available upon request to tepper@physics.usyd.edu.au.

[7] `http://www.physics.usyd.edu.au/~tepper/proj_galah_paper.html`

the coarse-grained potential is well behaved. The simulation includes a thick disc which is shown only in the vertical phase plane. Since the thick disc is older and more metal poor than the thin disc, including two discs allows us to study the predicted age and metallicity dependence of the cohent spiral. This is the base model we use to study the perturbation induced by an impactor.

In movie P2, we show the same configuration space for movie P1, but now each star is colour-coded by its azimuthal velocity V_ϕ in the plane of the disc. The velocity field reflects the underlying rotation curve consistent with the total gravitational potential. This becomes relevant when comparing to the perturbed cases below. There are small variations across the disc consistent with the stochastic spiral perturbations.

In movie P3, we show the evolution of the thin and thick discs in the vertical phase plane (z, V_z) coded by the azimuthal velocity V_ϕ, i.e. $V_\phi(z, V_z)$. There is no statistical averaging $\langle V_\phi \rangle$ over the population as carried out for the *Gaia* data (e.g. Figure 5). These are projections of the *entire* disc population and so are dominated by the inner disc with its higher V_z motions compressed in z. The different vertical thicknesses are evident and they remain fairly constant as the disc evolves in time. Relative to the Sun's location, each star undergoes clockwise motion about (z, V_z)=(0,0) as it oscillates in the disc potential with an angular frequency proportional to the vertical frequency ω_z where $\omega_z^2 = (1/z)\, d\Phi_z/dz$. The phase amplitude $\mathcal{A}_z$ is given by the star's energy and location in the disc potential (Figure 6). No coherent patterns emerge because the phases are randomised over 2π.

7.3 Perturbed model: hyperbolic orbit

At the same website (footnote 7), we present the interaction of the Galaxy with the intermediate-mass (S1) and high-mass (R1) impactors moving along a hyperbolic orbit (shown as a filled red circle) crossing the disc at about $R = 13$ kpc. After time $t = 95$ Myr, the disc undergoes an upwards displacement towards the approaching impactor and its centre of mass experiences a recoil. By the time the impactor has transited the disc plane, the entire disc has responded to the perturber. By $t = 180$ Myr, the interaction has excited a spiral arm and a strong warp in the outer disc that precesses in the plane around the centre of mass (cf. Gómez et al. 2015). The upwards momentum of the disc does not reverse until after $t = 400$ Myr. The strong forcing by the perturber is active for less than 100 Myr but the disc response persists for the 2 Gyr duration of the movie. For reference, the results are also shown in Figure 16 and Figure 17 respectively at a single timestep ($t = 900$ Myr).

In Figure 16 (R2) and Figure 17 (S2), when compared to the isolated Galaxy model (movie P2), the azimuthal velocity field V_ϕ shows systematic variations due to the low-amplitude bending waves (corrugations or wrinkles) propagating through the disc. The kinematically distinct, azimuthal 'plumes' (confined in radius) arise from disc segments displaced vertically by varying amounts, with larger displacements resulting in bigger lags with respect to the disc rotation at that radius. In other words, these kinematic plumes are mostly associated with large V_z motion and some V_R motion.

In Figure 16 (R3) and Figure 17 (S3), these same kinematic plumes encoded with the same V_ϕ velocities manifest in the (z, V_z) plane. For example, we show plumes at two different radii for a single timestep ($t = 900$ Myr). In R3, the spiral feature at 10 kpc aligns and elongates with the disc whereas the feature in the outer disc appears more circular as expected from theory (Figure 6).

At times, a one-armed spiral feature is clear (e.g. movies S3 and R3 during $1.2 < t < 1.9$ Gyr) although tracing it to the origin in (z, V_z) proves to be difficult without the action analysis (Section 4) applied directly to the models (Tepper-García et al. 2019). This is because our sampling (limited by N_P) is not sufficient to provide contrast against the clockwise population from the dominant underlying disc. In the absence of another disc-transiting event, these spiral features can be long-lived ($\gtrsim 500$ Myr) in the vertical phase plane.

In Figure 16, for the high-mass impactor (R3), there are several coherent one-armed plumes in the (z, V_z) plane. Once again, these grow to their maximum amplitude in $|z_{\rm max}| \approx 6$ kpc and $|V_{z_{\rm max}}| \approx 60$ km s^{-1} long after the transit has occurred. This appears to be associated with the strong vertical recoil of the disc after its reversal along the impactor's orbit. In particular, note the coherent *elliptic* plume aligned with and encircling the disc ($V_z < 0$) emerging at $t = 900$ Myr and persisting for 100 Myr. The low value of $\mathcal{A}_z$ (Figure 6) reinforces that this feature occurs at smaller radius ($R \approx 13 - 15$ kpc). There are spiral plumes down to maybe $R \approx 10$ kpc but insufficiently populated to give good contrast. This is a failing of the current models. Much larger simulations with an order of magnitude more particles are already under way.

In Figure 17, for the intermediate-mass impactor (S3), we see the kinematic spiral has lower amplitude in both axes. It grows out of the disc, rotates as a fixed pattern, reaching its maximum amplitude in $|z_{\rm max}| \approx 2.5$-3 kpc and $|V_{z_{\rm max}}| \approx 30 - 40$ km s^{-1}. In Figure 17 (S4), the vertical phase plane is encoded with the Galactocentric radius R: we see that the coherent spiral patterns occur at $R \approx 15 - 20$ kpc. (These features may also be associated with the reversal of the disc's momentum parallel to the impactor's orbit.) We note that $|z_{\rm max}|$ and $|V_{z_{\rm max}}|$ approximately match the predicted values in Figure 6 at $R = 20$ kpc; the model effectively "calibrates" the expected amplitudes at other radii, in particular the anticipated values of $|z_{\rm max}| \approx 1$ kpc and $|V_{z_{\rm max}}| \approx 50$ km s^{-1} at $R \approx R_\odot$ (Antoja et al. 2018). We see the effects of the spiral phase at lower radii down to 10 kpc but the contrast is poor.

In Figure 16 (R4), the strongest spiral phase signal is further out at $R \approx 20$ kpc. The outer disc of the Galaxy must be experiencing a strong forced oscillation, with stars confined to well-defined corrugations or wrinkles (Schönrich & Dehnen 2018). This is a strong prediction of our simulations given the low-flying orbit of Sgr over the disc. It seems reasonable to consider that this is the explanation for the TriAndromeda and Monoceros "rings" discovered by the SDSS survey towards the outer stellar disc (Xu et al. 2015) and maybe even most of the wave-like structure, ripples and corrugations claimed to date (Schönrich & Dehnen 2018).

7.4 Perturbed model: realistic orbit

In movie M1 (footnote 7), we present our model for the low-mass Sgr impact along a realistic orbit (see Tepper-García & Bland-Hawthorn 2018). Contemporary models agree that Sgr initially crossed the disc along a trajectory perpendicular to the Galactic plane (e.g. Law et al. 2005; Purcell et al. 2011). But at late times, as the orbit became circularised by dynamical friction (e.g. Jiang & Binney 2000), the trajectory evolved to be more inclined to the disc ($i \lesssim 30°$), and therefore less impulsive. The last crossing occurred at a radius of about $R \approx 13$ kpc.

All of the movies from Model M look very similar to the unperturbed case (Model P), with the exception of one. When we compare model M3 to the stable model P3 for the thin disc, there is clear evidence of heating in the former due to the action of the low-mass perturber. Such dynamical heating can happen over the disc where

the forcing frequency is out of phase with the intrinsic disc response. This heating also occurs in the high-mass and intermediate-mass cases but this is obscured by the dramatic plumes arising from the disc.

In movies L and K (footnote 7), we present our model for the intermediate and high mass impacts respectively along essentially the same orbit. In Figure 18, we show frames from movie K4 at two different timesteps, 30 Myr before and 90 Myr after a disc transit. This is to emphasise how clean the spiral phase signature is right before impact, and how it is wiped out for up to $\approx 100 - 150$ Myr after the impact, reforming thereafter.

In Figure 18(e), there are three distinct spiral phase patterns arising in three radial bins ($R = 17, 15, 12$ kpc). We can calibrate the strength of the signal in Antoja et al. (2018) from our numerical simulations, confirmed by the single crossing hyperbolic models. The low-mass impactor (Model M) barely ruffles the disc. The high-mass impactor (Model K) produces features with $|z_{\rm max}| \lesssim 5$ kpc and $|V_{z_{\rm max}}| \lesssim 50$ km s $^{-1}$, comparable to the results for the high-mass hyperbolic case (Model R). The intermediate-mass case scales down as it did for the hyperbolic models, thus consistent with the amplitude of the Antoja spiral at $R = R_\odot$. In movie K5, we show the spiral phase pattern also occurs in $V_R(z, V_z)$ for the same features observed in $V_\phi(z, V_z)$, albeit with less contrast.

After impact, the spiral features do arise again from the ashes and are persistent until the next impact. The fact that we see a clear spiral phase today is consistent with the passage of time since the last crossing about 400 Myr ago (by general consensus) and our imminent disc crossing in $\gtrsim$50 Myr. This makes the spiral phenomenon no older than about 250 Myr.

7.5 Velocity ellipsoid

To demonstrate the signature of a velocity ellipsoid in phase space, we extract a similar volume observed by Siebert et al. (2008) from the same impactor simulations. By construction, in our model $\langle \sigma_R \sigma_z \rangle \equiv 0$ (see above). We therefore add by hand a tilt of $\pm 7.2^\circ$ to match the tilt inferred from observations in a comparable range in z (Siebert et al. 2008). We measure the radial (V_R) and vertical (V_z) velocity of the stellar disc particles within an annulus of width 0.25 kpc centered at 8.25 kpc, within a range $\Delta z = 0.5$ kpc centered at $z = 0.5$ kpc and -0.5 kpc. In each case, we splatter the selected particles onto a V_z vs. V_R diagram. We bin the resulting distribution using 20 km s^{-1} bins along each axis, and smooth the 2D histogram with a narrow (5 km s^{-1}) Gaussian kernel. The result is shown in Fig. 14. We note that the final distribution is not overly sensitive to reasonable variations in the bin size and kernel width.

8 DISCUSSION

Antoja et al. (2018) argue that the beautiful spiral in the vertical phase plane discovered by *Gaia* arises from the response of the Galactic disc to a massive transiting system some time in the past 850 Myr. Through the use of simulations, we argue the feature arises from a complex process that must be investigated in detail. Inter alia, we believe the coherent spiral structure to be much younger than stated. In support of this, Binney & Schoenrich (2018) has provided an impulsive model that couples the actions in all dimensions and leads to a shorter age (200 Myr) for the spiral.

Alternative explanations. There are other dynamical processes that can give rise to a coherent spiral but these require contrived conditions. Candlish et al. (2014) gave a mechanism involving phase wrapping from popping star clusters embedded in a disc potential. Their original proposal was aimed at explaining a thick disc arising from massive ancient clusters that became unbound (Kroupa 2002; Assmann et al. 2011). They considered three baryonic cluster masses ($10^5, 10^6, 10^7 M_\odot$) embedded within a Miyamoto-Nagai disc and demonstrate well-defined spiral phase structure under idealized conditions. Once the star cluster is allowed to orbit with the time-varying restoring force from the disk, the coherence is largely washed out in one rotation period. We consider this model to be unlikely because the thick disc is ancient ($\gtrsim$10 Gyr) and we have already shown (Section 3.2) the spiral phase reflects the metallicity gradient in R and z with no evidence for a population restricted in metallicity or age. Likewise, if the idea is that a massive local starburst was triggered by one of the disc crossings, most of the popping star clusters would be described by a random distribution of temporal phases over 100 Myr that would smear out the signal (Bland-Hawthorn et al. 2010). Since clusters are born in the galactic plane, the vertical phase plane would also show bisymmetry, i.e. $(z, V_z) = (-z, -V_z)$, which is not observed. In any event, there is no evidence from the GALAH spectra for a coherent spiral pattern built up from a burst population.

Model predictions. The dynamical models in Section 6 make a number of important predictions: (1) after a disc transit, sufficient time ($\gtrsim$ 100 Myr) is needed for the coherent spiral phase through the bending waves across the disc to develop. (2) The early disc response after transit is "driven" because of the grazing incidence of Sgr's orbit. (3) Since the last transit was about 400 Myr ago by general consensus, the coherent fossil signature we see today can only be about 250 Myr old. (4) If there is no subsequent transit, the spiral phase can persist for at least 500 Myr. (5) We do not expect a strong signature in [Fe/H] because stars at all z-heights appear to get thoroughly mixed in the process. This was our motivation in Section 6 for considering a cool stellar disk embedded in the thick disc prior to the impact of Sgr. As we see in the movie sequences for Models K, L and M (footnote 7), there is no clear distinction in the vertical phase plane between the thin and thick disk stars. Since the spiral phase population (high V_ϕ) comprise of order 10% of the stars by volume, it may be difficult to separate these from the background population, especially over the inner disc.

Reaching the solar neighbourhood. Most of the coherent action in our simulations occurs in the range $10 < R < 20$ kpc. Inside $R \approx 10$ kpc, we were unable to detect this signature cleanly in either the cold or warm disc components (Section 6). We investigated three kinds of sampling of the simulations, i.e. circumferential binning over 2π, quadrant binning over $\pi/2$ at two different rotations separated by $\pi/4$, and individual samples matched to our survey volume. Binning over too large a region wipes out the signal, particularly in galactocentric radius. As we saw in Section 4, the clearest signal in the data comes from restricting the sample in radius to $|\Delta R - R_\odot| = 0.1$ kpc. But near the simulated solar neighbourhood, no clear signal emerged over Antoja's original volume. However, an action analyis as in Section 4 applied to the models is more revealing, e.g. the spiral phase is seen most strongly in stars with smaller radial actions (Tepper-García et al. 2019).

Two issues that come to mind are insufficient resolution (particle separation) and coarseness (particle density), both of which can affect the contrast and coherence of the spiral phase pattern. The former is less of a problem because the spiral phase is sufficiently broad along its length ($\delta\psi/\psi \lesssim 1/4$), particularly at large r_{ps}. In some samples, we were able to pick out features of this approximate width but not with any spirality. But the coarseness imposed by discs

Table 1. Galaxy model parameters. Column headers are as follows: $M_{\rm t}$:= total mass (10^9 M$_\odot$); $r_{\rm s}$:= scalelength (kpc); $r_{\rm tr}$:= truncation radius (kpc); $N_{\rm p}$:= number of particles (10^5).

	Profile	$M_{\rm t}$	$r_{\rm s}$	$r_{\rm tr}$	$N_{\rm p}$
Galaxy					
DM halo	H	10^3	38.4	250	10
Bulge	H	9	0.7	4	3
Thick disc	MN	20	5.0[a]	20	6
Thin disc	Exp/Sech	28	5.0[b]	20	10

Notes. H := Hernquist (1990) profile; MN := Miyamoto & Nagai (1975) profile; Exp := radial exponential profile.; Sech := vertical sech$^2 z$ profile.
[a] scaleheight set to 0.5 kpc.
[b] scaleheight set to 0.3 kpc.

with $N \sim 10^6$ particles may limit our sensitivity to fine structure, in contrast to spherical simulations where the problem would not arise (Sellwood 2013). Coarseness leads to collisional relaxation through scattering that is amplified at fixed N in flat distributions (Rybicki 1972). The usual formula

$$\tau_{\rm relax} = \frac{N}{6 \ln N} \tau_{\rm dyn}, \quad (15)$$

for which the dynamical time $\tau_{\rm dyn}$ is much shorter than the relaxation (scattering) timescale $\tau_{\rm relax}$, must be modified by a complicated factor of order 10^{-4} (Sellwood 2013) such that $\tau_{\rm relax} \sim \tau_{\rm dyn}$ in our application. But here we employ the adaptive mesh refinement scheme (Section 6) which obviates the impact of close encounters by design. In our set up, each cell over which the gravitational force is calculated is guaranteed to have enough particles (25) such that 2-body interactions are mostly negligible. This is confirmed by our base model (e.g. movie P4 for the cold thin disk) which exhibits only marginal evidence for heating (footnote 7).

Future work. It is not obvious that, given our parameters, we would have missed a coherent settling population at $R = R_\odot$ within our impactor simulations. Much larger simulations (i.e. $N \sim 10^8$ particles per Galactic component) are now under way to explore the issue more thoroughly; we report on these results in a follow-up paper. We look closely at the impulsive approximation for an orthogonal impact (Binney & Schoenrich 2018) for how coupling arises across the three phase planes (R, V_R; z, V_z; ϕ, V_ϕ). We compare the predictions to our Sgr model with its steep-angle transit crossing (with respect to the x, y and z axes) to see if this manifests as a strong coupling in 6D phase space. We study how much of the forced oscillation goes into heating the disc, particularly in regions which cannot keep up with the forcing frequency. This phenomenon was seen in the Sgr impactor models across the thin disc in particular (Section 7). Ultimately, we seek to provide a deeper understanding of the coherent spiral phase, and what it teaches us about the seismology of the Galactic disc.

Table 2. Overview of impactor models. Column headers are as follows: $M_{\rm tot}$:= total mass (10^9 M$_\odot$); $M_{\rm tid}$:= tidal mass (10^9 M$_\odot$); $r_{\rm tr}$:= truncation radius (kpc); $N_{\rm p}$:= number of particles (10^5). The last column gives the approximate initial orbital speed (km s^{-1}). See the notes below the table for more information.

Model	$M_{\rm tot}$	$M_{\rm tid}$	$r_{\rm tr}$	$N_{\rm p}$	v_0
P (no impactor)	–	–	–	–	–
R (high mass, single cross)	100	60	24	2	370
S (intermediate mass, single cross)	50	30	19	1	360
T (low mass, single cross)	10	5	12	1	350
K (high mass, Sgr orbit)	100	90	60	5	80
L (intermediate mass, Sgr orbit)	50	40	45	5	80
M (low mass, Sgr orbit)	10	7	25	5	80

Notes. An impactor consists of a 4×10^8 M$_\odot$ Hernquist stellar spheroid with a scale radius of 0.85 kpc and truncation radius of 2.5 kpc, embedded in a Hernquist DM subhalo with a scale radius of 10 kpc, a mass and radial extent as given above. For models R, S and T, the impactor is placed on a hyperbolic orbit around the Galaxy characterised by an eccentricity $e = 1.3$ and pericentric distance of 10 kpc, at an initial position with respect to the Galactic Centre of $R \approx (21, 45)$ kpc. The extent ($r_{\rm tr}$) corresponds roughly to the tidal radius at 50 kpc from a 10^{12} M$_\odot$ host. The tidal mass is the mass enclosed within $r_{\rm tr}$. For models K, L and M, the impactor is placed at an initial distance $d = 125$ kpc from the Galactic centre, and follows a 'trefoil' orbit as expected in most infall models (see Tepper-García & Bland-Hawthorn 2018, and Figure 15). The extent ($r_{\rm tr}$) corresponds roughly to the tidal radius at 125 kpc from a 10^{12} M$_\odot$ host.

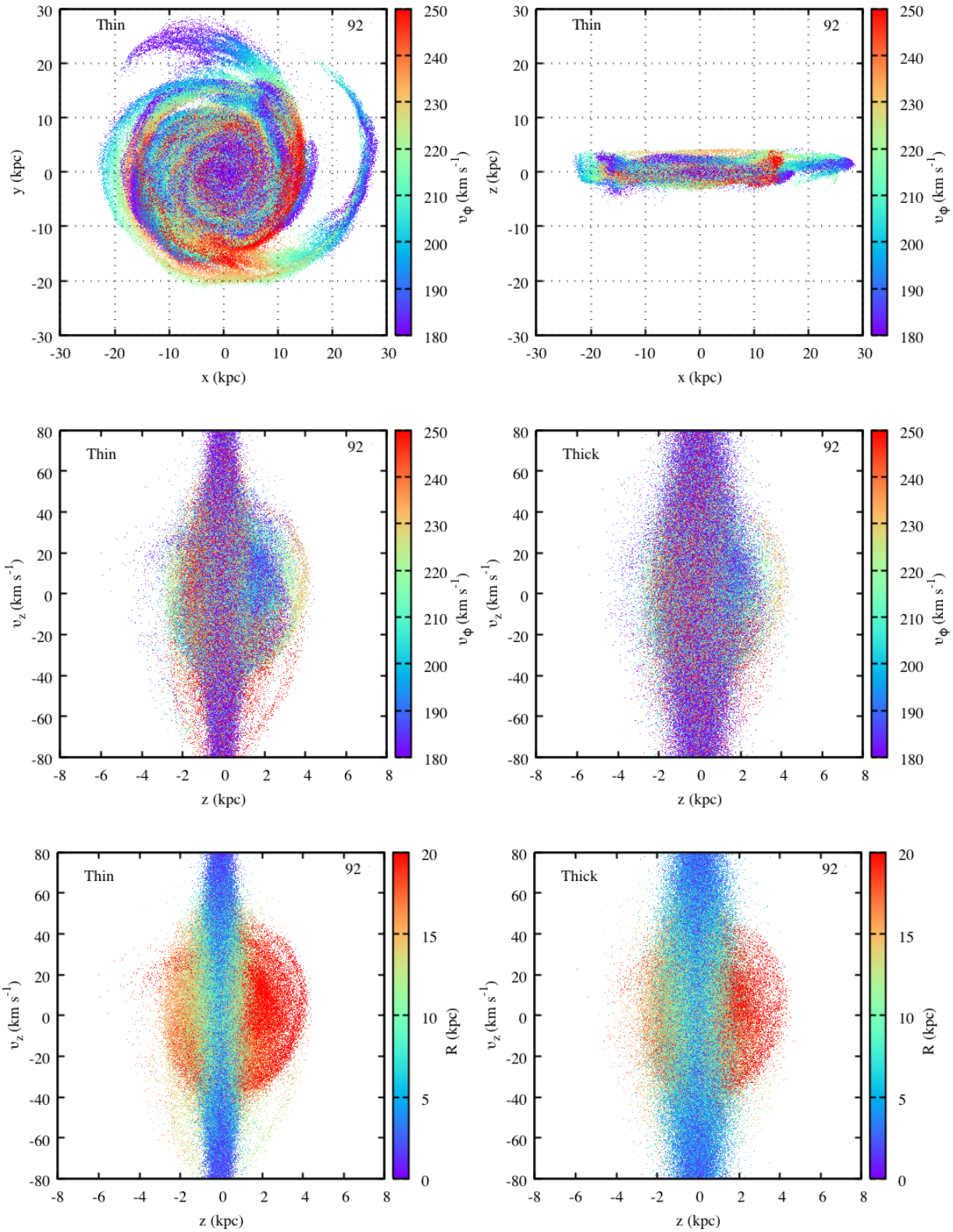

Figure 16. Simulated results for the high mass impactor (Model R; footnote 7) on a hyperbolic orbit where only the Galaxy is shown. (a) x-y plane for the thin disc where the particles are colour coded with V_ϕ (Movie R2). (b) x-z plane for the thin disc where the particles are colour coded with V_ϕ (Movie R2). (c) $z - V_z$ vertical phase plane for the thin disc colour coded with V_ϕ (Movie R3). (d) $z - V_z$ vertical phase plane for the thick disc colour coded with V_ϕ (Movie R3). (e) $z - V_z$ vertical phase plane for the thin disc colour coded with R (Movie R4). (f) $z - V_z$ vertical phase plane for the thick disc colour coded with R (Movie R4). Note the coherent V_ϕ velocity structures, especially in configuration space and their interrelation across all phase planes, mostly due to strong V_z and weaker V_R motions. The thick disc shows the same extent and structure as the thin disc if one allows for order of magnitude fewer particles. In the vertical phase plane $V_\phi(z, V_z)$ in (c) and (e), there are coherent one-armed phase structures occurring at the same time (t = 92 Myr) near 20 kpc (red) and 10 kpc (green).

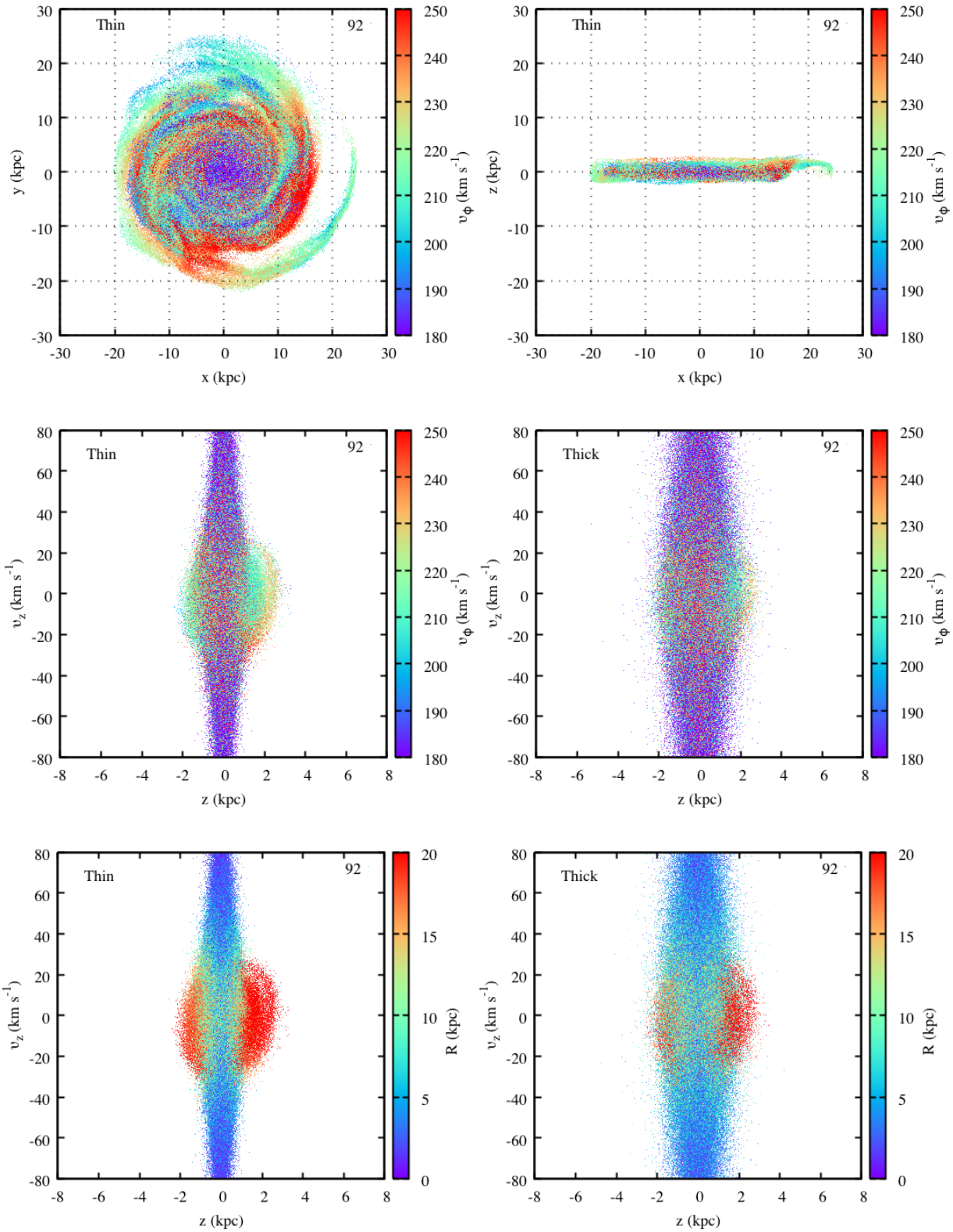

Figure 17. Simulated results for the intermediate mass impactor (Model S; footnote 7) on a hyperbolic orbit where only the Galaxy is shown. (a) x-y plane for the thin disc where the particles are colour coded with V_ϕ (Movie S2). (b) x-z plane for the thin disc where the particles are colour coded with V_ϕ (Movie S2). (c) $z - V_z$ vertical phase plane for the thin disc colour coded with V_ϕ (Movie S3). (d) $z - V_z$ vertical phase plane for the thick disc colour coded with V_ϕ (Movie S3). (e) $z - V_z$ vertical phase plane for the thin disc colour coded with R (Movie S4). (f) $z - V_z$ vertical phase plane for the thick disc colour coded with R (Movie S4). Once again, there are coherent velocity structures across all phase planes (t = 92 Myr). Now the physical and kinematic extent have both declined by almost a factor of two, consistent with the lower impactor mass. In (e), the one-armed spiral phase at 20 kpc is still apparent. The inner spiral phase pattern at R = 10 kpc is no longer visible.

ACKNOWLEDGEMENTS

This work has made use of data from the European Space Agency (ESA) mission *Gaia* (https://www.cosmos.esa.int/gaia), processed by the *Gaia* Data Processing and Analysis Consortium (DPAC, https://www.cosmos.esa.int/web/gaia/dpac/consortium). This work is also based on data acquired from the Australian Astronomical Telescope. We acknowledge the traditional owners of the land on which the AAT stands, the Gamilaraay people, and pay our respects to elders past and present.

JBH is supported by an ARC Australian Laureate Fellowship and the ARC Centre of Excellence for All Sky Astrophysics in 3 Dimensions (ASTRO-3D) through project number CE170100013. SS is funded by a Dean's University Fellowship and through the Laureate Fellowship, which also supports TTG and GDS. MJH is supported by an ASTRO-3D Fellowship. JK is supported by a Discovery Project grant from the Australian Research Council (DP150104667) awarded to JBH and TB.

SB and KL acknowledge funds from the Alexander von Humboldt Foundation in the framework of the Sofja Kovalevskaja Award endowed by the Federal Ministry of Education and Research. SB, MA and KL acknowledge travel support from Universities Australia and Deutsche Akademische Austauschdienst. The research by MA, LD, JL, AMA, and DN has been supported by an Australian Research Council Laureate Fellowship to MA (grant FL110100012). LD gratefully acknowledges a scholarship from Zonta International District 24 and support from ARC grant DP160103747. LD, KF and Y-ST are grateful for support from Australian Research Council grant DP160103747. KL acknowledges funds from the Swedish Research Council (Grant nr. 2015-00415_3) and Marie Sklodowska Curie Actions (Cofund Project INCA 600398). SLM acknowledges support from the Australian Research Council through grant DE140100598. LC is the recipient of an ARC Future Fellowship (project number FT160100402). GT, KČ, and TZ acknowledge the financial support from the Slovenian Research Agency (research core funding No. P1-0188). DMN is supported by the Allan C. and Dorothy H. Davis Fellowship. MŽ acknowledges support from ARC grant DP170102233. DS is the recipient of an ARC Future Fellowship (project number FT140100147).

JBH & TTG acknowledge the Sydney Informatics Hub and the University of Sydney's high performance computing (HPC) cluster Artemis for providing the HPC resources that have contributed to the some of the research results reported within this paper. Parts of this project were undertaken with the assistance of resources and services from the National Computational Infrastructure (NCI), which is supported by the Australian Government.

REFERENCES

Adibekyan V. Z., Sousa S. G., Santos N. C., Delgado Mena E., González Hernández J. I., Israelian G., Mayor M., Khachatryan G., 2012, A&A, 545, A32
Antoja T., et al., 2018, preprint, (arXiv:1804.10196)
Assmann P., Fellhauer M., Kroupa P., Brüns R. C., Smith R., 2011, MNRAS, 415, 1280
Barden S. C., et al., 2010, in Ground-based and Airborne Instrumentation for Astronomy III. p. 773509, doi:10.1117/12.856103
Binney J., McMillan P., 2011, MNRAS, 413, 1889
Binney J., Schoenrich R., 2018, preprint, (arXiv:1807.09819)
Binney J., Tremaine S., 2008, Galactic Dynamics: Second Edition. Princeton University Press
Binney J., et al., 2014, MNRAS, 439, 1231
Bland-Hawthorn J., Gerhard O., 2016, ARA&A, 54, 529
Bland-Hawthorn J., Sharma S., 2016, in van de Weygaert R., Shandarin S., Saar E., Einasto J., eds, IAU Symposium Vol. 308, The Zeldovich Universe: Genesis and Growth of the Cosmic Web. pp 561–570, doi:10.1017/S1743921316010589
Bland-Hawthorn J., Krumholz M. R., Freeman K., 2010, ApJ, 713, 166
Bovy J., 2015, ApJS, 216, 29
Brown A. G. A., Vallenari A., Prusti T., de Bruijne J. H. J., Babusiaux C., Bailer-Jones C. A. L., 2018, preprint, (arXiv:1804.09365)
Büdenbender A., van de Ven G., Watkins L. L., 2015, MNRAS, 452, 956
Buder S., et al., 2018, preprint, (arXiv:1804.06041)
Candlish G. N., Smith R., Fellhauer M., Gibson B. K., Kroupa P., Assmann P., 2014, MNRAS, 437, 3702
Carollo D., et al., 2010, ApJ, 712, 692
Chequers M. H., Widrow L. M., Darling K., 2018, preprint, (arXiv:1805.12449)
De Silva G. M., et al., 2015, MNRAS, 449, 2604
Deng L.-C., et al., 2012, Research in Astronomy and Astrophysics, 12, 735
Eyer L., et al., 2018, preprint, (arXiv:1804.09382)
Freeman K., Bland-Hawthorn J., 2002, ARA&A, 40, 487
Freeman K., Bland-Hawthorn J., 2008, in Kodama T., Yamada T., Aoki K., eds, Astronomical Society of the Pacific Conference Series Vol. 399, Panoramic Views of Galaxy Formation and Evolution. p. 439
Gómez F. A., Besla G., Carpintero D. D., Villalobos Á., O'Shea B. W., Bell E. F., 2015, ApJ, 802, 128
Gravity Collaboration et al., 2018, A&A, 615, L15
Hayden M. R., et al., 2015, ApJ, 808, 132
Hernquist L., 1990, ApJ, 356, 359
Hernquist L., 1993, ApJS, 86, 389
Hori G., Liu T. P., 1963, PASJ, 15, 101
Hunter C., Toomre A., 1969, ApJ, 155, 747
Ibata R. A., Wyse R. F. G., Gilmore G., Irwin M. J., Suntzeff N. B., 1997, AJ, 113, 634
Ida S., Kokubo E., Makino J., 1993, MNRAS, 263, 875
Jeans J. H., 1915, MNRAS, 76, 70
Jiang I.-G., Binney J., 2000, MNRAS, 314, 468
Kazantzidis S., Magorrian J., Moore B., 2004, ApJ, 601, 37
Koppelman H. H., Helmi A., Veljanoski J., 2018, preprint, (arXiv:1804.11347)
Kos J., et al., 2017, MNRAS, 464, 1259
Kos J., et al., 2018, preprint, (arXiv:1807.00822)
Kroupa P., 2002, MNRAS, 330, 707
Law D. R., Johnston K. V., Majewski S. R., 2005, ApJ, 619, 807
Lynden-Bell D., 1962, MNRAS, 124, 279
Lynden-Bell D., 1967, MNRAS, 136, 101
Malhan K., Ibata R. A., Martin N. F., 2018, preprint, (arXiv:1804.11339)
Marchetti T., Rossi E. M., Brown A. G. A., 2018, preprint, (arXiv:1804.10607)
Martell S. L., et al., 2017, MNRAS, 465, 3203
Masset F., Tagger M., 1997a, A&A, 318, 747
Masset F., Tagger M., 1997b, A&A, 322, 442
McMillan P. J., 2011, MNRAS, 414, 2446
McMillan P. J., Binney J. J., 2008, MNRAS, 390, 429
Miyamoto M., Nagai R., 1975, PASJ, 27, 533
Ollongren A., 1962, Bull. Astron. Inst. Netherlands, 16, 241
Perret V., Renaud F., Epinat B., Amram P., Bournaud F., Contini T., Teyssier R., Lambert J.-C., 2014, A&A, 562, A1
Perryman M. A. C., et al., 2001, A&A, 369, 339
Prusti T., et al., 2016, A&A, 595, A1
Purcell C. W., Bullock J. S., Tollerud E. J., Rocha M., Chakrabarti S., 2011, Nature, 477, 301
Reid M. J., Brunthaler A., 2004, ApJ, 616, 872
Rybicki G. B., 1972, in Lecar M., ed., Astrophysics and Space Science Library Vol. 31, IAU Colloq. 10: Gravitational N-Body Problem. p. 22, doi:10.1007/978-94-010-2870-7_4
Saha K., Jog C. J., 2006, MNRAS, 367, 1297
Salo H., Laurikainen E., 2000, MNRAS, 319, 393
Sanders J., 2012, MNRAS, 426, 128
Schönrich R., Dehnen W., 2018, MNRAS, 478, 3809

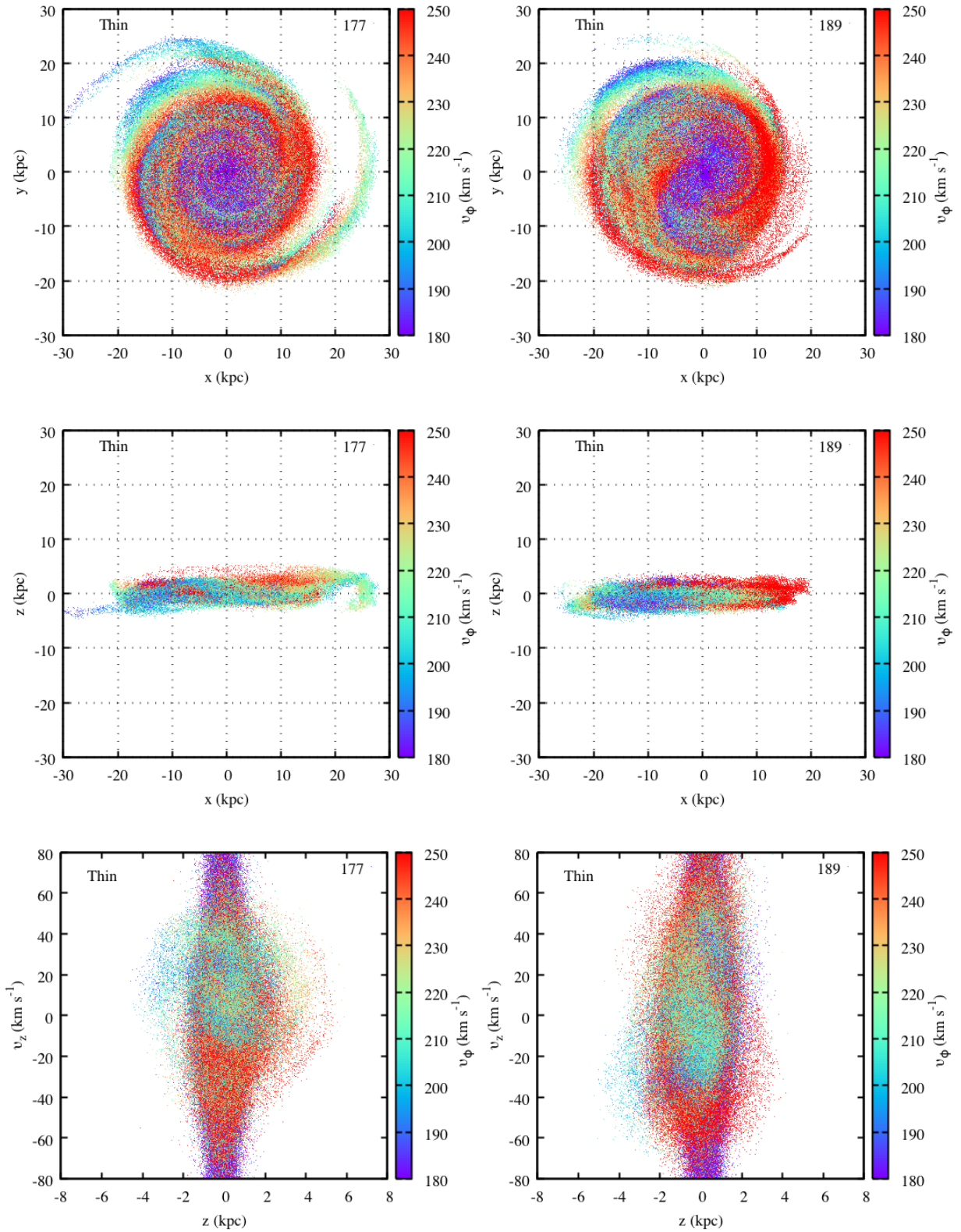

Figure 18. Simulated results for the high mass impactor (Model K; footnote 7) on a realistic Sgr orbit where only the Galaxy is shown. We present results for just before and just after the last disc transit which occurred at 1.8 Gyr in the simulation. (a) x-y plane for the thin disc 30 Myr *before* transit where the particles are colour coded with V_ϕ. (b) same as in (a) but 90 Myr *after* the disc crossing. (c) x-z plane for the thin disc 30 Myr *before* transit where the particles are colour coded with V_ϕ. (d) same as in (c) but 90 Myr *after* the disc crossing. (e) $z - V_z$ plane 30 Myr *before* the disc crossing. (f) same as (e) but 90 Myr *after* the disc crossing. Note how the coherent phase space structures in (e) are wiped out in (f); the extent in z is also compressed right after the disc transit such that the pattern must rebuild from scratch. Weaker related one-armed structures are seen in $V_R(z, V_z)$ as we observe in the accompanying simulations (Movie K5; footnote 7).

Sellwood J. A., 2013, ApJ, 769, L24
Sellwood J. A., Carlberg R. G., 1984, ApJ, 282, 61
Sellwood J. A., Carlberg R. G., 2014, ApJ, 785, 137
Sharma S., Bland-Hawthorn J., Johnston K. V., Binney J., 2011, ApJ, 730, 3
Sharma S., et al., 2014, ApJ, 793, 51
Sharma S., et al., 2018, MNRAS, 473, 2004
Sheinis A., et al., 2015, Journal of Astronomical Telescopes, Instruments, and Systems, 1, 035002
Siebert A., et al., 2008, MNRAS, 391, 793
Springel V., Di Matteo T., Hernquist L., 2005, MNRAS, 361, 776
Sridhar S., Touma J., 1996, MNRAS, 279, 1263
Tepper-García T., Bland-Hawthorn J., 2018, MNRAS, 478, 5263
Tepper-García T., Bland-Hawthorn J., Binney J., Sharma S., GALAH team 2019, preprint (arXiv:in preparation)
Terquem C. E. J. M. L. J., 1998, ApJ, 509, 819
Teyssier R., 2002, A&A, 385, 337
Toomre A., 1964, ApJ, 139, 1217
Wittenmyer R. A., et al., 2018, AJ, 155, 84
Xu Y., Newberg H. J., Carlin J. L., Liu C., Deng L., Li J., Schönrich R., Yanny B., 2015, ApJ, 801, 105
Zasov A. V., Zaitseva N. A., 2017, Astronomy Letters, 43, 439
Zwitter T., et al., 2018, preprint, (arXiv:1804.06344)

[1]Sydney Institute for Astronomy, School of Physics, A28, The University of Sydney, NSW 2006, Australia
[2]Center of Excellence for Astrophysics in Three Dimensions (ASTRO-3D), Australia
[3]Miller Professor, Miller Institute, University of California Berkeley, CA 94720, USA
[4]Rudolf Peierls Centre for Theoretical Physics, Clarendon Laboratory, Oxford, OX1 3PU, UK
[5]Research School of Astronomy & Astrophysics, Australian National University, ACT 2611, Australia
[6]Department of Physics and Astronomy, Macquarie University, Sydney, NSW 2109, Australia
[7]Max Planck Institute for Astronomy (MPIA), Koenigstuhl 17, 69117 Heidelberg, Germany
[8]Fellow of the International Max Planck Research School for Astronomy & Cosmic Physics at the University of Heidelberg, Germany
[9]Department of Physics and Astronomy, Uppsala University, Box 516, SE-751 20 Uppsala, Sweden
[10]School of Physics, UNSW, Sydney, NSW 2052, Australia
[11]Department of Astronomy, Columbia University, Pupin Physics Laboratories, New York, NY 10027, USA
[12]Center for Computational Astrophysics, Flatiron Institute, 162 Fifth Avenue, New York, NY 10010, USA
[13]Faculty of Mathematics and Physics, University of Ljubljana, Jadranska 19, 1000 Ljubljana, Slovenia

This paper has been typeset from a TEX/LATEX file prepared by the author.